Journal of the Mechanics and Physics of Solids 57 (2009) 1391–1416

Contents lists available at ScienceDirect

Journal of the Mechanics and Physics of Solids

journal homepage: www.elsevier.com/locate/jmps

On electromagnetic forming processes in finitely strained solids: Theory and examples

J.D. Thomas, N. Triantafyllidis *

The University of Michigan, Aerospace Engineering Department, Ann Arbor, MI 48109-2140, USA

ARTICLE INFO

Article history:
Received 29 August 2008
Received in revised form
23 March 2009
Accepted 2 April 2009

Keywords:
Electromechanical processes
Finite strain
Finite elements
Numerical algorithms
Variational calculus

ABSTRACT

The process of electromagnetic forming (EMF) is a high velocity manufacturing technique that uses electromagnetic (Lorentz) body forces to shape sheet metal parts. EMF holds several advantages over conventional forming techniques: speed, repeatability, one-sided tooling, and most importantly considerable ductility increase in several metals. Current modeling techniques for EMF processes are not based on coupled variational principles to simultaneously account for electromagnetic and mechanical effects. Typically, separate solutions to the electromagnetic (Maxwell) and motion (Newton) equations are combined in staggered or lock-step methods, sequentially solving the mechanical and electromagnetic problems.

The present work addresses these issues by introducing a fully coupled Lagrangian (reference configuration) least-action variational principle, involving magnetic flux and electric potentials and the displacement field as independent variables. The corresponding Euler–Lagrange equations are Maxwell's and Newton's equations in the reference configuration, which are shown to coincide with their current configuration counterparts obtained independently by a direct approach. The general theory is subsequently simplified for EMF processes by considering the eddy current approximation.

Next, an application is presented for axisymmetric EMF problems. It is shown that the proposed variational principle forms the basis of a variational integration numerical scheme that provides an efficient staggered solution algorithm. As an illustration a number of such processes are simulated, inspired by recent experiments of freely expanding uncoated and polyurea-coated aluminum tubes.

© 2009 Elsevier Ltd. All rights reserved.

1. Introduction

Electromagnetic forming (EMF) is a high velocity sheet metal forming technique that is receiving renewed attention due to a number of advantages it offers over conventional forming. In EMF a large capacitor bank is connected in series with a forming coil (typically a copper wire solenoid). Discharging the capacitor bank through the coil results in a large transient current, which in turn induces electric currents in the nearby metallic workpiece. The resulting Lorentz forces cause workpiece plastic deformation, with a characteristic process time on the order of 50 μs. The input electric energy can be precisely controlled, making the process repeatable, and the non-contact loading allows the use of single side tooling (an advantage in the forming of parts that are already coated on one side). However, the most prominent advantage is a significant increase in workpiece ductility over conventional techniques (Balanethiram and Daehn, 1992, 1994; Imbert et al., 2005a, b; Seth and Daehn, 2005; Seth et al., 2005), though the mechanism behind this increase is still being debated (Zhang and Ravi-Chandar, 2006, 2008a, b).

* Corresponding author.
E-mail address: nick@umich.edu (N. Triantafyllidis).

0022-5096/$ - see front matter © 2009 Elsevier Ltd. All rights reserved.
doi:10.1016/j.jmps.2009.04.004

Predictive modeling of EMF and other coupled electromagnetic–mechanical processes has been a topic of extensive research in recent years. One approach, applicable to simple—typically axisymmetric—geometries, that involves the use of semi-analytical techniques was used for ring expansion by Gourdin (1989) and Triantafyllidis and Waldenmyer (2004) and for plate bulging by Takatsu et al. (1988). This approach relies on known integration forms and inductance formulas. However, it cannot be generalized to arbitrary geometries.

For the case of more general geometries, EMF problems are solved by using either loose coupling of separate electromagnetic and mechanical solvers or a staggered approach where a unified code solves separately the electromagnetic and mechanical (and thermal) problems at each solution step. Often commercial finite element method (FEM) codes form the basis of such solution schemes, as in the work of Oliveira et al. (2005), Karch and Roll (2005), and L'Eplattenier et al. (2006). Reviews of different coupled techniques for EMF solutions are given in El-Azab et al. (2003), Kleiner et al. (2004), and Svendsen and Chanda (2005). Stiemer et al. (2006) introduced a finite element methodology specifically to solve electromagnetic–mechanical problems (see also Reese et al., 2005; Svendsen and Chanda, 2005; Unger et al., 2006). A slightly different approach that uses the arbitrary Lagrangian–Eulerian (ALE) framework was employed by Fenton and Daehn (1998) to simulate EMF plate bulging, and a related staggered scheme in the ALE framework was given by Rieben et al. (2006). However, all these techniques solve separately the electromagnetic and the mechanical boundary value problems and lack a consistent variational foundation.

The present work's goal is to propose a fully coupled theory for electromagnetic–mechanical processes, specifically in the context of EMF. Electromagnetic–mechanical modeling has been studied by several researchers. Although a detailed literature review is beyond the scope of this paper, one should mention at this point the extensive development for coupled electromagnetic–mechanical processes in the books by Maugin (1988), Eringen and Maugin (1990), and Kovetz (2000). In this work we seek a variational principle whose Euler–Lagrange equations are Maxwell's and Newton's equations. A consistent variational formulation of the electromagnetic problem in deformable solids was introduced by Lax and Nelson (1976), who derived Maxwell's equations, interface conditions, and the corresponding electromagnetic Lagrangian terms in the reference configuration. In the work of Maugin (1993) (revisited in the more recent work of Trimarco and Maugin, 2001; Trimarco, 2007), mechanical terms augment the electromagnetic Lagrangian terms. Upon applying Hamilton's principle, the corresponding Euler–Lagrange equations are Maxwell's equations and the mechanical equation of motion. This approach is presently modified for EMF problems using the eddy current approximation, which results in a new variational (Hamilton's) principle. Following this step, a variational integration algorithm, applied to the proposed Hamilton's principle, produces a staggered solution approach.

The discussion begins in Section 2 with a derivation of the coupled electromagnetic–mechanical equations. Section 2.1 presents the derivation in the current configuration, using the conservation laws (Kovetz, 2000). In Section 2.2 the reference configuration form of these equations and the electromagnetic fields is derived using a method similar to that of Lax and Nelson (1976). The resulting relations between current and reference configuration fields allow the introduction of the electromagnetic–mechanical Lagrangian, which is used for the least-action principle in Section 2.3. Section 3 proposes the variational principle for the eddy current approximation and discusses its restriction to axisymmetric forming cases. The numerical solution algorithm is derived using a variational integration technique, as outlined in Section 4. In Section 5, results of several cases of tube expansion simulations are presented. Finally, Section 6 gives a critical discussion of the proposed formulation and its numerical implementation, along with suggestions for future work, and Section 7 concludes the presentation.

2. Formulation of fully coupled electromagnetic–thermal–mechanical problem

Two methods for deriving the fully coupled governing equations and interface conditions of an electromagnetic–thermal–mechanical process are presented.[1] First is the direct method, which uses conservation principles in the current configuration to derive the governing equations and boundary conditions. This approach essentially follows Kovetz (2000), where the interested reader is referred to for additional details. Subsequently, kinematic relations from continuum mechanics are applied to transform the governing equations from the current to the reference configuration.

Using the relations between current and reference configuration fields, the second, variational method is presented, based on a least-action principle (for the purely electromagnetic case see Lax and Nelson, 1976) in the reference configuration. The corresponding Euler–Lagrange equations in the reference configuration are shown to agree with their current configuration counterparts obtained via the direct approach.

2.1. Conservation law approach (current configuration)

Gauss' law states electric charge conservation in an arbitrary control volume $v(t)$ that is allowed to move and deform following the material. Electric charge conservation dictates

$$\int_{\partial v(t)} \boldsymbol{d} \bullet \boldsymbol{n}\, \mathrm{d}s = \int_{v(t)} q\, \mathrm{d}v, \tag{2.1}$$

[1] Dyadic notation is employed with bold face letters denoting vectors or tensors, $\bullet$ denoting tensor contraction, and $\times$ denoting the vector product.

where $\partial v(t)$ is the surface boundary of the control volume $v(t)$, $\boldsymbol{n}$ is the outward normal to the surface $\partial v(t)$, $\boldsymbol{d}$ is the electric displacement, and q is the volumetric electric charge. The pointwise form of Gauss' equation and the associated interface condition follow from the arbitrariness of the control volume and standard arguments involving Gauss' divergence theorem, namely

$$\nabla \bullet \boldsymbol{d} = q, \quad \boldsymbol{n} \bullet [\![\boldsymbol{d}]\!] = 0, \tag{2.2}$$

where $[\![\ ]\!]$ denotes the jump in a quantity across an interface. For simplicity, and without loss of generality, it is assumed from here on that all electric charges and currents within the problem domain are volumetric.

Faraday's induction law states that the circulation of the electromotive intensity $\mathscr{E}$ about a closed circuit $\partial s(t)$ opposes the change of the flux of the magnetic field $\boldsymbol{b}$ through the surface $s(t)$, i.e.

$$\oint_{\partial s(t)} \mathscr{E} \bullet \boldsymbol{s}\, \mathrm{d}l = -\frac{\mathrm{d}}{\mathrm{d}t} \int_{s(t)} \boldsymbol{b} \bullet \boldsymbol{n}\, \mathrm{d}s, \tag{2.3}$$

where $\partial s(t)$ is the line boundary of the control surface $s(t)$, $\boldsymbol{s}$ is the tangent vector to $\partial s(t)$, and $\boldsymbol{n}$ is the normal to the surface directed positively using the right-hand rule applied to $\boldsymbol{s}$ on $\partial s(t)$. Again, since the control surface is arbitrary, the pointwise form of Faraday's equation and the associated interface condition follow by using standard arguments involving Stokes' theorem

$$\nabla \times \mathscr{E} = -\overset{*}{\boldsymbol{b}}, \quad \boldsymbol{n} \times [\![\mathscr{E}]\!] = \boldsymbol{0}, \tag{2.4}$$

where $\overset{*}{(\,)}$ denotes the flux derivative. Note that since the control volume or surface may move and deform, the conservation laws must be Galilean invariant. The electric displacement $\boldsymbol{d}$ and magnetic field $\boldsymbol{b}$ are Galilean invariant, as is the electromotive intensity $\mathscr{E}$, which is defined in terms of the non-Galilean invariant electric field $\boldsymbol{e}$, magnetic field $\boldsymbol{b}$, and material point velocity[2] $\dot{\boldsymbol{u}}$ by

$$\mathscr{E} \equiv \boldsymbol{e} + \dot{\boldsymbol{u}} \times \boldsymbol{b}, \tag{2.5}$$

where $\dot{(\,)} \equiv \mathrm{d}()/\mathrm{d}t$ denotes the material time derivative. The relation between current position $\boldsymbol{x}$, reference position $\boldsymbol{X}$, and displacement $\boldsymbol{u}$ of a material point is

$$\boldsymbol{x} = \boldsymbol{X} + \boldsymbol{u}. \tag{2.6}$$

Recall that the flux derivative for any vector field $\boldsymbol{f}$ is defined by

$$\overset{*}{\boldsymbol{f}} \equiv \frac{\partial \boldsymbol{f}}{\partial t} + \dot{\boldsymbol{u}}(\nabla \bullet \boldsymbol{f}) - \nabla \times (\dot{\boldsymbol{u}} \times \boldsymbol{f}) = \dot{\boldsymbol{f}} - (\dot{\boldsymbol{u}} \nabla) \bullet \boldsymbol{f} + \boldsymbol{f}(\nabla \bullet \dot{\boldsymbol{u}}) \tag{2.7}$$

and satisfies

$$\frac{\mathrm{d}}{\mathrm{d}t} \int_{s(t)} \boldsymbol{f} \bullet \boldsymbol{n}\, \mathrm{d}s = \int_{s(t)} \overset{*}{\boldsymbol{f}} \bullet \boldsymbol{n}\, \mathrm{d}s, \tag{2.8}$$

thus justifying the pointwise form of Faraday's law in Eq. $(2.4)_1$.

The non-existence of magnetic charge in integral form is expressed by

$$\int_{\partial v(t)} \boldsymbol{b} \bullet \boldsymbol{n}\, \mathrm{d}s = 0. \tag{2.9}$$

The pointwise equation and interface condition follow as in the case of Gauss' law in Eq. (2.2),

$$\nabla \bullet \boldsymbol{b} = 0, \quad \boldsymbol{n} \bullet [\![\boldsymbol{b}]\!] = 0. \tag{2.10}$$

The fourth and final electromagnetic conservation law is Ampere's equation, which states that the circulation of the magnetomotive intensity $\mathscr{H}$ about a closed circuit $\partial s(t)$ is equal to the total current flux through the surface $s(t)$ which is bounded by $\partial s(t)$,

$$\oint_{\partial s(t)} \mathscr{H} \bullet \boldsymbol{s}\, \mathrm{d}l = \frac{\mathrm{d}}{\mathrm{d}t} \int_{s(t)} \boldsymbol{d} \bullet \boldsymbol{n}\, \mathrm{d}s + \int_{s(t)} \mathscr{J} \bullet \boldsymbol{n}\, \mathrm{d}s. \tag{2.11}$$

The first term on the right-hand side of Eq. (2.11) is the displacement current flux through $s(t)$ while the second term accounts for the induction current. As expected from the time dependence of the control surface, the magnetomotive intensity $\mathscr{H}$ and the conduction current density $\mathscr{J}$ are both Galilean invariant. Similar arguments to those used for the Faraday law in Eq. (2.4) lead to the pointwise form of Ampere's equation and the associated interface condition, namely

$$\nabla \times \mathscr{H} = \overset{*}{\boldsymbol{d}} + \mathscr{J}, \quad \boldsymbol{n} \times [\![\mathscr{H}]\!] = \boldsymbol{0}. \tag{2.12}$$

[2] The material point velocity is usually denoted by $\boldsymbol{v}(\boldsymbol{x}, t)$ in an Eulerian description and by $\dot{\boldsymbol{u}}(\boldsymbol{X}, t)$ in a Lagrangian description. In the interest of notational simplicity, material point velocity is hereon denoted solely by $\dot{\boldsymbol{u}}$.

Note that according to the simplifying assumption discussed at the beginning of this subsection there is no surface electric current taken into account. The magnetomotive intensity $\mathscr{H}$ and conduction current density $\mathscr{J}$ are defined as

$$\mathscr{H} \equiv \boldsymbol{h} - \dot{\boldsymbol{u}} \times \boldsymbol{d}, \quad \mathscr{J} \equiv \boldsymbol{j} - q\,\dot{\boldsymbol{u}}, \tag{2.13}$$

where $\boldsymbol{h}$ is the H field and $\boldsymbol{j}$ is the electric current density.[3]

In addition to the four electromagnetic conservation laws, five additional principles are needed, three from mechanics and two from thermodynamics. First is conservation of mass, which in integral form states

$$\frac{\mathrm{d}}{\mathrm{d}t}\int_{v(t)} \rho \,\mathrm{d}v = 0, \tag{2.14}$$

where ρ is the mass density. The arbitrariness of the control volume, which always follows the same set of material points, yields the pointwise equation

$$\dot{\rho} + \rho(\nabla \bullet \dot{\boldsymbol{u}}) = 0. \tag{2.15}$$

For simplicity, it is assumed here and subsequently that all discontinuities propagate at the speed of the material. Consequently no jump condition is needed for mass conservation.

The next mechanics principle is that of conservation of linear momentum, generalized for the electromagnetic–mechanical system. In integral form this is given by

$$\frac{\mathrm{d}}{\mathrm{d}t}\int_{v(t)} \rho\boldsymbol{g} \,\mathrm{d}v = \int_{v(t)} \rho\boldsymbol{f} \,\mathrm{d}v + \int_{\partial v(t)} \boldsymbol{t} \,\mathrm{d}s, \tag{2.16}$$

where $\boldsymbol{g}$ is the generalized electromagnetic–mechanical momentum (to be specified subsequently), $\boldsymbol{f}$ is the mechanical body force, and $\boldsymbol{t}$ is the generalized electromagnetic–mechanical traction on the surface of the control volume (also to be specified subsequently). It is further assumed that Cauchy's formula relates the electromagnetic–mechanical surface traction $\boldsymbol{t}$ to $\boldsymbol{\sigma}$, the generalized electromagnetic–mechanical (Maxwell) stress,

$$\boldsymbol{t} = \boldsymbol{n} \bullet \boldsymbol{\sigma}. \tag{2.17}$$

The pointwise form of the conservation of linear momentum and the associated interface condition follow from the arbitrariness of the control volume, by using standard arguments which involve Gauss' divergence theorem,

$$\rho\,\dot{\boldsymbol{g}} = \nabla \bullet \boldsymbol{\sigma} + \rho\boldsymbol{f}, \quad \boldsymbol{n} \bullet [\![\,\boldsymbol{\sigma}\,]\!] = \boldsymbol{t}, \tag{2.18}$$

where $\boldsymbol{t}$ in the jump condition is the applied mechanical surface traction.

The third mechanics principle is the conservation of angular momentum, generalized for the electromagnetic–mechanical system, which states[4]

$$\frac{\mathrm{d}}{\mathrm{d}t}\int_{v(t)} \boldsymbol{x} \wedge \rho\boldsymbol{g} \,\mathrm{d}v = \int_{v(t)} \boldsymbol{x} \wedge \rho\boldsymbol{f} \,\mathrm{d}v + \int_{\partial v(t)} \boldsymbol{x} \wedge \boldsymbol{t} \,\mathrm{d}s. \tag{2.19}$$

The pointwise form follows from the arbitrariness of the control volume and the use of mass and linear momentum conservation in Eqs. (2.15) and (2.18)

$$\rho\,\dot{\boldsymbol{u}} \wedge \boldsymbol{g} = \boldsymbol{\sigma}^T - \boldsymbol{\sigma}. \tag{2.20}$$

Note that no associated interface condition is needed since all interfaces propagate at the speed of the material.

The first thermodynamic principle pertains to the balance of power, which states that the rate of change of the control volume's total energy is equal to the power supplied externally, i.e.

$$\begin{aligned}\frac{\mathrm{d}}{\mathrm{d}t}\int_{v(t)} \rho\varepsilon \,\mathrm{d}v = &\int_{v(t)} \rho\boldsymbol{f} \bullet \dot{\boldsymbol{u}} \,\mathrm{d}v + \int_{\partial v(t)} \boldsymbol{t} \bullet \dot{\boldsymbol{u}} \,\mathrm{d}s \\ &+ \int_{v(t)} \rho h \,\mathrm{d}v + \int_{\partial v(t)} (-\boldsymbol{q}) \bullet \boldsymbol{n} \,\mathrm{d}s \\ &+ \int_{\partial v(t)} (-\mathscr{E} \times \mathscr{H}) \bullet \boldsymbol{n} \,\mathrm{d}s,\end{aligned} \tag{2.21}$$

where ε is the specific total energy. The first line in the right-hand side of Eq. (2.21) is the supplied mechanical power, where the first term is the body force contribution and the second term is the surface traction contribution. The second line in the right-hand side of Eq. (2.21) is the supplied thermal power, where the first term accounts for internal heating and the second term accounts for surface heating. The specific rate of heating, i.e. the rate of heating per mass, is denoted by h, and the heat flux through the surface is denoted by $\boldsymbol{q}$ and is oriented such that a positive value indicates heat flux out of the

[3] The fields $\boldsymbol{b}$ and $\boldsymbol{h}$ are denoted here as the magnetic field and H field, respectively. In the literature they are also referred to as the magnetic flux and magnetic field, respectively, and $\boldsymbol{h}$ is often denoted as the current potential (Kovetz, 2000).

[4] Recall that the wedge product of two vectors is defined as $\boldsymbol{a} \wedge \boldsymbol{b} \equiv \boldsymbol{ab} - \boldsymbol{ba}$.

control volume.[5] Finally, the third line in the right-hand side of Eq. (2.21) is the supplied electromagnetic power through the surface. The electromagnetic energy flux is given by the Poynting vector $\mathscr{E}\times\mathscr{H}$, again oriented such that a positive value indicates energy flux out of the control volume. The pointwise form of the energy balance and the associated interface condition follow once again from the arbitrariness of the control volume using standard arguments involving Gauss' divergence theorem, namely

$$\begin{aligned}&\rho\,\dot{\varepsilon}=\rho(\boldsymbol{f}\bullet\dot{\boldsymbol{u}}+h)+\nabla\bullet(\boldsymbol{\sigma}\bullet\dot{\boldsymbol{u}}-\boldsymbol{q}-\mathscr{E}\times\mathscr{H}),\\&\boldsymbol{n}\bullet[\![-\boldsymbol{\sigma}\bullet\dot{\boldsymbol{u}}+\boldsymbol{q}+\mathscr{E}\times\mathscr{H}]\!]=0.\end{aligned}\tag{2.22}$$

The second thermodynamic principle is the entropy production inequality, which states that the rate of change of the control volume's entropy must be greater than or equal to the entropy supplied to it, i.e.

$$\frac{\mathrm{d}}{\mathrm{d}t}\int_{v(t)}\rho s\,\mathrm{d}v\geqslant\int_{v(t)}\rho\frac{h}{T}\,\mathrm{d}v+\int_{\partial v(t)}\left(\frac{-\boldsymbol{q}}{T}\right)\bullet\boldsymbol{n}\,\mathrm{d}s,\tag{2.23}$$

where s is the specific entropy[6] and T is the absolute temperature. The first term in the right-hand side of Eq. (2.23) accounts for the entropy supplied by the internal heating, and the second term accounts for the entropy supplied by the heat flux through the surface of the control volume. The integral form provides, through the same arguments used for the energy balance in Eq. (2.22), the pointwise entropy production inequality and associated jump condition,

$$\rho\,\dot{s}\geqslant\frac{\rho h}{T}+\nabla\bullet\left(\frac{-\boldsymbol{q}}{T}\right),\quad\boldsymbol{n}\bullet[\![\frac{\boldsymbol{q}}{T}]\!]\geqslant0.\tag{2.24}$$

With the necessary balance laws in place, the method of Coleman and Noll (1963) is used to find the material's constitutive laws. In order to do so, one needs first the electromagnetic constitutive laws in the current configuration. For simplicity, and motivated by the EMF applications of interest, it is assumed that the magnetization and polarization of the material are negligible and hence

$$\boldsymbol{d}=\varepsilon_0\boldsymbol{e},\quad\boldsymbol{h}=\frac{1}{\mu_0}\boldsymbol{b},\tag{2.25}$$

where ε_0 is the permittivity of free space and μ_0 is the permeability of free space. The next piece of information required pertains to the specific free energy ψ, which is defined by (Kovetz, 2000)

$$\rho\psi\equiv\rho\varepsilon-T\rho s-\rho(\boldsymbol{g}\bullet\dot{\boldsymbol{u}})+\frac{\rho}{2}(\dot{\boldsymbol{u}}\bullet\dot{\boldsymbol{u}})-\frac{\varepsilon_0}{2}(\boldsymbol{e}\bullet\boldsymbol{e})-\frac{1}{2\mu_0}(\boldsymbol{b}\bullet\boldsymbol{b})+(\boldsymbol{d}\times\boldsymbol{b})\bullet\dot{\boldsymbol{u}}.\tag{2.26}$$

This states that ψ equals the specific total energy less the energy due to thermal, kinetic, and electromagnetic sources (the expression in Eq. (2.26) also accounts that there is no polarization or magnetization in the material).

For the case of non-magnetizable and non-polarizable materials, it is assumed that the specific free energy[7]

$$\psi=\psi(\boldsymbol{F},T,\boldsymbol{\xi}),\tag{2.27}$$

where $\boldsymbol{F}$ is the deformation gradient, $\boldsymbol{F}\equiv\partial\boldsymbol{x}/\partial\boldsymbol{X}$, and $\boldsymbol{\xi}$ are—mechanical in nature—internal variables. From the pointwise energy balance in Eq. (2.22) the expression for ρh is substituted into the entropy production inequality. Rearranging the result using Eqs. (2.15), (2.25), and (2.26), the pointwise entropy production inequality (2.24) can be rewritten as[8]

$$\begin{aligned}&\left[\boldsymbol{\sigma}^T-\rho\left(\frac{\partial\psi}{\partial\boldsymbol{F}}\right)\bullet\boldsymbol{F}^T+\varepsilon_0\left(\frac{1}{2}(\boldsymbol{e}\bullet\boldsymbol{e})\boldsymbol{I}-\boldsymbol{e}\boldsymbol{e}\right)+\frac{1}{\mu_0}\left(\frac{1}{2}(\boldsymbol{b}\bullet\boldsymbol{b})\boldsymbol{I}-\boldsymbol{b}\boldsymbol{b}\right)-(\boldsymbol{d}\times\boldsymbol{b})\dot{\boldsymbol{u}}\right]\vdots(\dot{\boldsymbol{u}}\nabla)-\rho\left[\frac{\partial\psi}{\partial T}+s\right]\dot{T}-[\rho\boldsymbol{g}-\rho\,\dot{\boldsymbol{u}}-\boldsymbol{d}\times\boldsymbol{b}]\bullet\ddot{\boldsymbol{u}}\\&\quad-\rho\left(\frac{\partial\psi}{\partial\boldsymbol{\xi}}\right)\bullet\dot{\boldsymbol{\xi}}+\mathscr{J}\bullet\mathscr{E}+\left(\frac{-\boldsymbol{q}}{T}\right)\bullet\nabla T\geqslant0.\end{aligned}\tag{2.28}$$

This inequality must hold for any admissible thermodynamic process, i.e. for arbitrary $\dot{\boldsymbol{u}}\nabla$, $\dot{T}$, and $\ddot{\boldsymbol{u}}$, which implies that the terms grouped in brackets multiplying these arbitrary quantities must be zero. The vanishing of the term multiplying $\dot{\boldsymbol{u}}\nabla$ provides the electromagnetic–mechanical stress expression sought

$$\boldsymbol{\sigma}=\rho\boldsymbol{F}\bullet\left(\frac{\partial\psi}{\partial\boldsymbol{F}}\right)^T+\varepsilon_0\left(\boldsymbol{e}\boldsymbol{e}-\frac{1}{2}(\boldsymbol{e}\bullet\boldsymbol{e})\boldsymbol{I}\right)+\frac{1}{\mu_0}\left(\boldsymbol{b}\boldsymbol{b}-\frac{1}{2}(\boldsymbol{b}\bullet\boldsymbol{b})\boldsymbol{I}\right)+\dot{\boldsymbol{u}}(\boldsymbol{d}\times\boldsymbol{b}).\tag{2.29}$$

[5] The reader must not confuse the scalar specific rate of heating h with the vector H field $\boldsymbol{h}$ nor the vector heat flux $\boldsymbol{q}$ with the scalar volumetric charge q.

[6] The reader must not confuse the scalar specific entropy s with the line tangent vector $\boldsymbol{s}$.

[7] In general, ψ is taken as a function of $\boldsymbol{F}$, T, $\boldsymbol{\xi}$, $\dot{\boldsymbol{u}}$, $\mathscr{E}$, $\boldsymbol{B}$, and ∇T. For details, see Kovetz (2000) and Svendsen and Chanda (2005).

[8] Double tensor contraction in dyadic notation $\boldsymbol{A}\vdots\boldsymbol{B}\equiv A_{ij}B_{ij}$.

The electromagnetic–mechanical stress can be divided into mechanical, $\boldsymbol{\sigma}_m$, and electromagnetic, $\boldsymbol{\sigma}_{em}$, parts

$$\begin{aligned}
&\boldsymbol{\sigma} = \boldsymbol{\sigma}_m + \boldsymbol{\sigma}_{em},\\
&\boldsymbol{\sigma}_m \equiv \rho \boldsymbol{F} \bullet \left(\frac{\partial \psi}{\partial \boldsymbol{F}}\right)^T,\\
&\boldsymbol{\sigma}_{em} \equiv \varepsilon_0 \left(\boldsymbol{e}\boldsymbol{e} - \frac{1}{2}(\boldsymbol{e} \bullet \boldsymbol{e})\boldsymbol{I}\right) + \frac{1}{\mu_0}\left(\boldsymbol{b}\boldsymbol{b} - \frac{1}{2}(\boldsymbol{b} \bullet \boldsymbol{b})\boldsymbol{I}\right) + \dot{\boldsymbol{u}}(\boldsymbol{d} \times \boldsymbol{b}).
\end{aligned} \tag{2.30}$$

The vanishing of the term multiplying $\dot{T}$ in Eq. (2.28) provides the entropy relation

$$s = -\frac{\partial \psi}{\partial T}, \tag{2.31}$$

while the vanishing of the term multiplying $\ddot{\boldsymbol{u}}$ in Eq. (2.28) provides the electromagnetic–mechanical momentum relation

$$\boldsymbol{g} = \dot{\boldsymbol{u}} + \frac{1}{\rho}(\boldsymbol{d} \times \boldsymbol{b}). \tag{2.32}$$

One can now verify using Eqs. (2.29) and (2.32) that the angular momentum balance in Eq. (2.20) is satisfied.

It is further assumed that the mechanical dissipation term, which involves the internal variables in Eq. (2.28), satisfies the independent restriction

$$-\rho\left(\frac{\partial \psi}{\partial \boldsymbol{\xi}}\right) \bullet \dot{\boldsymbol{\xi}} \geqslant 0. \tag{2.33}$$

Here $-\rho\partial\psi/\partial\boldsymbol{\xi}$ is the work conjugate thermodynamic driving force associated to $\boldsymbol{\xi}$. The constitutive equations must be complemented by the evolution laws for $\dot{\boldsymbol{\xi}}$ (for examples in metal plasticity the interested reader is referred to the book by Lubliner, 1990).

Upon taking into account Eqs. (2.29), (2.31), (2.32), and the restriction on the mechanical dissipation in (2.33) the final form of the entropy inequality equation (2.28) is the following statement about the ohmic and thermal dissipation

$$\mathscr{J} \bullet \mathscr{E} + \left(\frac{-\boldsymbol{q}}{T}\right) \bullet \nabla T \geqslant 0. \tag{2.34}$$

Substituting for $\boldsymbol{g}$ from Eq. (2.32) into the pointwise linear momentum equation (2.18) one obtains

$$\nabla \bullet \boldsymbol{\sigma} + \rho \boldsymbol{f} = \rho \frac{\mathrm{d}}{\mathrm{d}t}\left(\frac{1}{\rho}(\boldsymbol{d} \times \boldsymbol{b})\right) + \rho \ddot{\boldsymbol{u}}. \tag{2.35}$$

Using the definition of $\boldsymbol{\sigma}$ from Eq. (2.29), and Maxwell's equations (2.2), (2.4), (2.10), and (2.12), the above equation of motion may be further simplified to the more physically transparent form

$$\nabla \bullet \boldsymbol{\sigma}_m + \boldsymbol{j} \times \boldsymbol{b} + q\boldsymbol{e} + \rho \boldsymbol{f} = \rho \ddot{\boldsymbol{u}}, \tag{2.36}$$

which shows that the divergence of the mechanical stress $\boldsymbol{\sigma}_m$ plus the Lorentz force terms, $\boldsymbol{j} \times \boldsymbol{b} + q\boldsymbol{e}$, plus the mechanical body force $\rho\boldsymbol{f}$ equals the inertia term $\rho\ddot{\boldsymbol{u}}$. It is worth noting that the Lorentz force terms have appeared as a result of the generalized electromagnetic–mechanical stress, without assuming their existence a priori.

2.2. Transformation of field quantities from current to reference configuration

Kinematic relations from continuum mechanics are now used to obtain the relations between current and reference configuration fields and to transform the previous conservation laws to their reference configuration counterparts. To this end, one needs the three equations relating volume elements, oriented line elements, and oriented surface elements in the reference and current configurations (the last of which is Nanson's formula), namely[9]

$$\mathrm{d}v = J\mathrm{d}V, \quad \boldsymbol{s}\,\mathrm{d}l = (\boldsymbol{F} \bullet \boldsymbol{S})\,\mathrm{d}L, \quad \boldsymbol{n}\,\mathrm{d}s = J(\boldsymbol{N} \bullet \boldsymbol{F}^{-1})\,\mathrm{d}S, \quad J = \det(\boldsymbol{F}), \tag{2.37}$$

where $\boldsymbol{S}$ is the tangent to the line element $\mathrm{d}L$ in the reference configuration, and $\boldsymbol{N}$ is the normal to the surface element $\mathrm{d}S$ in the reference configuration.

Beginning with conservation of charge, Eq. (2.1), and using Eq. (2.37) to transform the integration from current to reference configuration yields

$$\int_{\partial V} (J\boldsymbol{F}^{-1} \bullet \boldsymbol{d}) \bullet \boldsymbol{N}\,\mathrm{d}S = \int_V Jq\,\mathrm{d}V. \tag{2.38}$$

[9] Here and subsequently capital letters will be used to designate field quantities in the reference configuration corresponding to the lowercase field in the current configuration.

This implies the definitions

$$\boldsymbol{D} \equiv J\boldsymbol{F}^{-1} \bullet \boldsymbol{d}, \quad Q \equiv Jq, \tag{2.39}$$

where $\boldsymbol{D}$ is the reference configuration electric displacement and Q is the reference configuration volume charge density. The pointwise Gauss' equation in the reference configuration and the interface condition follow from the arbitrariness of the reference configuration control volume using standard arguments as in the current configuration case in Eq. (2.2), namely

$$\boldsymbol{\nabla} \bullet \boldsymbol{D} = Q, \quad \boldsymbol{N} \bullet [\![\boldsymbol{D}]\!] = 0. \tag{2.40}$$

Whereas $\boldsymbol{\nabla}$ is the gradient operator in the current configuration, $\boldsymbol{\nabla}$ is the gradient operator in the reference configuration. Note that here and subsequently the reference configuration relations are simple to derive since the reference configuration is independent of time.

Next, the kinematic relations in Eq. (2.37) are applied to Faraday's law in Eq. (2.3), which yields

$$\oint_{\partial S} (\mathscr{E} \bullet \boldsymbol{F}) \bullet \boldsymbol{S}\, \mathrm{d}L = -\frac{\mathrm{d}}{\mathrm{d}t} \int_S (J\boldsymbol{F}^{-1} \bullet \boldsymbol{b}) \bullet \boldsymbol{N}\, \mathrm{d}S. \tag{2.41}$$

This leads to the definitions

$$\boldsymbol{E} \equiv \mathscr{E} \bullet \boldsymbol{F}, \quad \boldsymbol{B} \equiv J\boldsymbol{F}^{-1} \bullet \boldsymbol{b}, \tag{2.42}$$

where $\boldsymbol{E}$ is the electromotive intensity in the reference configuration and $\boldsymbol{B}$ is the magnetic field in the reference configuration. The pointwise Faraday's equation and associated interface condition in the reference configuration follow, similarly to the current configuration case,

$$\boldsymbol{\nabla} \times \boldsymbol{E} = -\dot{\boldsymbol{B}}, \quad \boldsymbol{N} \times [\![\boldsymbol{E}]\!] = \boldsymbol{0}. \tag{2.43}$$

Attention is focused next to the non-existence of magnetic charge, Eq. (2.9), which with the help of Eq. (2.37) gives in the reference configuration

$$\int_{\partial V} (J\boldsymbol{F}^{-1} \bullet \boldsymbol{b}) \bullet \boldsymbol{N}\, \mathrm{d}S = 0. \tag{2.44}$$

Using the previous definition for $\boldsymbol{B}$ in Eq. (2.42) leads to the pointwise statement and associated interface condition in the reference configuration,

$$\boldsymbol{\nabla} \bullet \boldsymbol{B} = 0, \quad \boldsymbol{N} \bullet [\![\boldsymbol{B}]\!] = 0. \tag{2.45}$$

The transformation of Ampere's law in the reference configuration comes from applying Eq. (2.37) to Eq. (2.11), yielding

$$\oint_{\partial S} (\mathscr{H} \bullet \boldsymbol{F}) \bullet \boldsymbol{S}\, \mathrm{d}L = \frac{\mathrm{d}}{\mathrm{d}t} \int_S (J\boldsymbol{F}^{-1} \bullet \boldsymbol{d}) \bullet \boldsymbol{N}\, \mathrm{d}S + \int_S (J\boldsymbol{F}^{-1} \bullet \mathscr{J}) \bullet \boldsymbol{N}\, \mathrm{d}S. \tag{2.46}$$

This leads to the definitions

$$\boldsymbol{H} \equiv \mathscr{H} \bullet \boldsymbol{F}, \quad \boldsymbol{J} \equiv J\boldsymbol{F}^{-1} \bullet \mathscr{J}, \tag{2.47}$$

where $\boldsymbol{H}$ is the magnetomotive intensity in the reference configuration and $\boldsymbol{J}$ is the conduction electric current density in the reference configuration.[10] With these definitions, the pointwise Ampere's equation and interface condition in the reference configuration follow in a similar fashion as for the current configuration case, Eq. (2.12),

$$\boldsymbol{\nabla} \times \boldsymbol{H} = \dot{\boldsymbol{D}} + \boldsymbol{J}, \quad \boldsymbol{N} \times [\![\boldsymbol{H}]\!] = \boldsymbol{0}. \tag{2.48}$$

Having established Maxwell's equations in the reference configuration attention is turned next to the mechanical conservation laws. The statement of conservation of mass, Eq. (2.14), is transformed to the reference configuration using Eq. (2.37),

$$\frac{\mathrm{d}}{\mathrm{d}t} \int_V J\rho \mathrm{d}V = 0, \tag{2.49}$$

which leads to the definition

$$\rho_0 \equiv J\rho, \tag{2.50}$$

where ρ_0 is the mass density in the reference configuration. The pointwise mass conservation equation in the reference configuration, counterpart of Eq. (2.15), is therefore

$$\dot{\rho}_0 = 0. \tag{2.51}$$

[10] The reader must not confuse the vector conduction electric current density in the reference configuration $\boldsymbol{J}$ with the scalar density for volume change $J = \det(\boldsymbol{F})$.

To find the relations between current and reference configuration stress and traction fields, one needs the conservation of linear momentum and Cauchy tetrahedron argument equation (2.17). Transforming Eqs. (2.16) and (2.17) with the help of Eq. (2.37) yields

$$\frac{\mathrm{d}}{\mathrm{d}t}\int_V J\rho\boldsymbol{g}\,\mathrm{d}V = \int_V J\rho\boldsymbol{f}\,\mathrm{d}V + \int_{\partial V}\boldsymbol{t}\frac{\mathrm{d}s}{\mathrm{d}S}\mathrm{d}S \tag{2.52}$$

and

$$\boldsymbol{T} = \boldsymbol{N}\bullet\boldsymbol{\Pi}. \tag{2.53}$$

This implies the definitions

$$\boldsymbol{T} \equiv \boldsymbol{t}\frac{\mathrm{d}s}{\mathrm{d}S}, \quad \boldsymbol{\Pi} \equiv J\boldsymbol{F}^{-1}\bullet\boldsymbol{\sigma}, \tag{2.54}$$

where $\boldsymbol{T}$ is the surface traction in the reference configuration[11] and $\boldsymbol{\Pi}$ is the electromagnetic–mechanical first Piola–Kirchhoff stress. Cauchy's formula (Eq. (2.17)) and Nanson's formula (Eq. $(2.37)_3$) lead to Eq. (2.53). With these definitions the pointwise equation of motion and corresponding interface condition in the reference configuration, which follow from Eqs. (2.52) to (2.54), in a similar fashion that Eq. (2.18) followed from Eqs. (2.16) and (2.17), are

$$\rho_0\dot{\boldsymbol{g}} = \boldsymbol{\nabla}\bullet\boldsymbol{\Pi} + \rho_0\boldsymbol{f}, \quad \boldsymbol{N}\bullet[\![\,\boldsymbol{\Pi}\,]\!] = \boldsymbol{T}. \tag{2.55}$$

The above derived reference configuration expressions for the current configuration field quantities introduced in Section 2.1 are the indispensable ingredients for the variational approach that follows.

2.3. Variational approach (reference configuration)

One of the most efficient ways to obtain Maxwell's equations, in the current configuration, through a variational approach (Hamilton's principle, see Lax and Nelson, 1976; Lazzari and Nibbi, 2000) is based on a potential formulation such that Faraday's equation, Eq. (2.4), and the statement of no magnetic charges, Eq. (2.10), are satisfied identically. A vector potential, $\boldsymbol{a}$, and scalar potential, ϕ, are defined such that

$$\boldsymbol{b} = \nabla\times\boldsymbol{a}, \quad \boldsymbol{e} = -\nabla\phi - \frac{\partial\boldsymbol{a}}{\partial t}. \tag{2.56}$$

The potentials in this formulation are not uniquely determined. A gauge condition must be applied for unique potentials, which will be discussed subsequently.

This potential formulation reduces the number of non-automatically satisfied Maxwell's equations to two. A purely electromagnetic Lagrangian density (i.e. excluding mechanical contributions) exists in terms of the generalized coordinates $\boldsymbol{a}$ and ϕ such that the Euler–Lagrange equations of the corresponding (Hamilton's) variational principle are Gauss' and Ampere's equations. This electromagnetic Lagrangian density is

$$\ell \equiv \frac{\varepsilon_0}{2}(\boldsymbol{e}\bullet\boldsymbol{e}) - \frac{1}{2\mu_0}(\boldsymbol{b}\bullet\boldsymbol{b}) + \boldsymbol{j}\bullet\boldsymbol{a} - q\phi, \tag{2.57}$$

where $\boldsymbol{e}$ and $\boldsymbol{b}$ are in terms of $\boldsymbol{a}$ and ϕ through Eq. (2.56).

In order to transform the current configuration electromagnetic Lagrangian density to its reference configuration counterpart, the vector and scalar potentials must be transformed accordingly. Substituting Eq. (2.42) into Eq. (2.56) yields after some manipulation (for details see Nelson, 1979)

$$\begin{aligned}\boldsymbol{B} &= \boldsymbol{\nabla}\times\boldsymbol{A},\\ \boldsymbol{E} &= -\boldsymbol{\nabla}\Phi - \dot{\boldsymbol{A}},\end{aligned} \tag{2.58}$$

where the reference configuration vector potential $\boldsymbol{A}$ and reference configuration scalar potential Φ are given in terms of their current configuration counterparts by

$$\begin{aligned}\boldsymbol{A} &\equiv \boldsymbol{a}\bullet\boldsymbol{F},\\ \Phi &\equiv \phi - \dot{\boldsymbol{u}}\bullet\boldsymbol{a}.\end{aligned} \tag{2.59}$$

As in the current configuration, the reference configuration potential formulation identically satisfies Faraday's equation, Eq. (2.43), and the statement of no magnetic charges, Eq. (2.45). Notice that these reference configuration potentials are still not unique, requiring a gauge condition.

With this formulation, the reference configuration Lagrangian for the full electromagnetic–mechanical case can now be obtained by adding the mechanical energy component to the electromagnetic part in Eq. (2.57). To achieve this one first

[11] The reader must not confuse the vector surface traction in the reference configuration $\boldsymbol{T}$ with the scalar temperature T.

needs to define the auxiliary term $\tilde{\boldsymbol{E}}$ as

$$\tilde{\boldsymbol{E}} \equiv \boldsymbol{E} - (\boldsymbol{F}^{-1} \bullet \dot{\boldsymbol{u}}) \times \boldsymbol{B}. \tag{2.60}$$

Then, given that the Lagrangian density ℓ transforms to the reference configuration as $J\ell$, adding the necessary mechanical energy terms, and substituting for the current configuration fields in terms of the reference configuration fields with the help of Eqs. (2.5), (2.13), (2.39), (2.42), (2.47), (2.59), and (2.60), yields the reference configuration Lagrangian

$$\begin{aligned}\mathscr{L} &\equiv \int_{\mathbb{R}^3} \left(J\ell + \rho_0 \left(\frac{1}{2}(\dot{\boldsymbol{u}} \bullet \dot{\boldsymbol{u}}) - \psi + \boldsymbol{f} \bullet \boldsymbol{u} \right) \right) \mathrm{d}V + \int_{\partial\Omega} \boldsymbol{T} \bullet \boldsymbol{u} \, \mathrm{d}S \\ &= \int_{\mathbb{R}^3} \left(\frac{\varepsilon_0 J}{2} (\tilde{\boldsymbol{E}} \bullet \boldsymbol{C}^{-1} \bullet \tilde{\boldsymbol{E}}) - \frac{1}{2\mu_0 J} (\boldsymbol{B} \bullet \boldsymbol{C} \bullet \boldsymbol{B}) + \boldsymbol{J} \bullet \boldsymbol{A} - Q\Phi + \rho_0 \left(\frac{1}{2}(\dot{\boldsymbol{u}} \bullet \dot{\boldsymbol{u}}) - \psi + \boldsymbol{f} \bullet \boldsymbol{u} \right) \right) \mathrm{d}V + \int_{\partial\Omega} \boldsymbol{T} \bullet \boldsymbol{u} \, \mathrm{d}S, \end{aligned} \tag{2.61}$$

where the independent fields are Φ, $\boldsymbol{A}$, and $\boldsymbol{u}$ and $\boldsymbol{C} \equiv \boldsymbol{F}^T \bullet \boldsymbol{F}$ is the right Cauchy–Green tensor. Here Ω is the domain occupied by the body, and $\partial\Omega$ is the surface of this body. Notice that the density $\rho_0(\boldsymbol{X}) \neq 0$ for $\boldsymbol{X} \in \Omega$ and $\rho_0(\boldsymbol{X}) = 0$ for $\boldsymbol{X} \in \mathbb{R}^3 \backslash \Omega$. Integration over $\mathbb{R}^3$ is necessary since electric and magnetic fields exist not only in the solid ($\boldsymbol{X} \in \Omega$) but also in its surrounding space ($\boldsymbol{X} \in \mathbb{R}^3 \backslash \Omega$). Φ and $\boldsymbol{u}$ are assumed continuous throughout $\mathbb{R}^3$, but only the tangent component of $\boldsymbol{A}$, i.e. $\boldsymbol{A}_t$, is assumed continuous across an interface. Moreover, note that $\boldsymbol{f}$, $\boldsymbol{T}$, $\boldsymbol{J}$, and Q in Eq. (2.61) are externally applied quantities and are held constant when taking variations under the subsequently discussed variational (Hamilton's) principle.

Hamilton's principle states that the action integral $\mathscr{F}$, defined as the integral of the Lagrangian introduced in Eq. (2.61) over the time interval $[t^1, t^2]$, is stationary[12]

$$\delta\mathscr{F} = 0, \quad \mathscr{F} \equiv \int_{t^1}^{t^2} \mathscr{L} \, \mathrm{d}t, \tag{2.62}$$

where $\delta\Phi = 0$, $\delta\boldsymbol{A} = \boldsymbol{0}$, and $\delta\boldsymbol{u} = \boldsymbol{0}$ at $t = t^1$ and $t = t^2$. The resulting Euler–Lagrange equations are the governing equations of the electromagnetic–mechanical system. More specifically:

Taking the variation of $\mathscr{F}$ with respect to Φ yields

$$\mathscr{F}_{,\Phi}[\delta\Phi] = \int_{t^1}^{t^2} \left\{ \int_{\mathbb{R}^3} (\boldsymbol{\nabla} \bullet (\varepsilon_0 J \tilde{\boldsymbol{E}} \bullet \boldsymbol{C}^{-1}) - Q) \delta\Phi \, \mathrm{d}V - \int_{\partial\Omega} [\![(\boldsymbol{N} \bullet (\varepsilon_0 J \tilde{\boldsymbol{E}} \bullet \boldsymbol{C}^{-1})) \delta\Phi]\!] \mathrm{d}S \right\} \mathrm{d}t = 0, \tag{2.63}$$

where integration by parts and Gauss' divergence theorem have been used. Using Eqs. (2.5), (2.25), (2.39), (2.42), and (2.60) one observes that the group of terms appearing in parenthesis in Eq. (2.63) is the reference configuration electric displacement

$$\boldsymbol{D} = \varepsilon_0 J \tilde{\boldsymbol{E}} \bullet \boldsymbol{C}^{-1}. \tag{2.64}$$

Consequently Eq. (2.63) implies

$$\boldsymbol{\nabla} \bullet \boldsymbol{D} = Q, \quad \boldsymbol{N} \bullet [\![\boldsymbol{D}]\!] = 0, \tag{2.65}$$

that is Gauss' equation and interface condition in the reference configuration, Eq. (2.40), as expected.

Taking the variation of $\mathscr{F}$ with respect to $\boldsymbol{A}$ gives

$$\begin{aligned}\mathscr{F}_{,\boldsymbol{A}}[\delta\boldsymbol{A}] = \int_{t^1}^{t^2} \Bigg\{ &\int_{\mathbb{R}^3} \left(\frac{\mathrm{d}}{\mathrm{d}t} (\varepsilon_0 J \tilde{\boldsymbol{E}} \bullet \boldsymbol{C}^{-1}) - \boldsymbol{\nabla} \times \left((\varepsilon_0 J \tilde{\boldsymbol{E}} \bullet \boldsymbol{C}^{-1}) \times (\boldsymbol{F}^{-1} \bullet \dot{\boldsymbol{u}}) + \frac{1}{\mu_0 J} (\boldsymbol{B} \bullet \boldsymbol{C}) \right) + \boldsymbol{J} \right) \bullet \delta\boldsymbol{A} \, \mathrm{d}V \\ &- \int_{\partial\Omega} [\![\left(\boldsymbol{N} \times \left((\varepsilon_0 J \tilde{\boldsymbol{E}} \bullet \boldsymbol{C}^{-1}) \times (\boldsymbol{F}^{-1} \bullet \dot{\boldsymbol{u}}) + \frac{1}{\mu_0 J} (\boldsymbol{B} \bullet \boldsymbol{C}) \right) \right) \bullet \delta\boldsymbol{A}]\!] \, \mathrm{d}S \Bigg\} \mathrm{d}t = 0, \end{aligned} \tag{2.66}$$

where integration by parts, identities for triple products, and Stoke's theorem have been used. Similarly to Eq. (2.64), using Eqs. (2.13), (2.25), (2.39), (2.42), and (2.47) one observes that the group of terms appearing in parenthesis in Eq. (2.66) is the reference configuration H field

$$\boldsymbol{H} = \frac{1}{\mu_0 J} (\boldsymbol{B} \bullet \boldsymbol{C}) - (\boldsymbol{F}^{-1} \bullet \dot{\boldsymbol{u}}) \times \boldsymbol{D}. \tag{2.67}$$

Consequently Eq. (2.66) yields[13]

$$\boldsymbol{\nabla} \times \boldsymbol{H} = \dot{\boldsymbol{D}} + \boldsymbol{J}, \quad \boldsymbol{N} \times [\![\boldsymbol{H}]\!] = \boldsymbol{0}, \tag{2.68}$$

which is Ampere's equation and the related interface condition, Eq. (2.48), in the reference configuration, again as expected.

Finally, the variation of $\mathscr{F}$ with respect to $\boldsymbol{u}$ will yield the equation of motion and surface traction condition in terms of the electromagnetic–mechanical momentum $\boldsymbol{g}$ and first Piola–Kirchhoff stress $\boldsymbol{\Pi}$. Applying integration by parts and Gauss'

[12] Here and subsequently δ denotes the variation of a functional.

[13] By the definitions of $\boldsymbol{N}$ and $\boldsymbol{A}_t$ one has $[\![(\boldsymbol{N} \times \boldsymbol{H}) \bullet \delta\boldsymbol{A}]\!] = (\boldsymbol{N} \times [\![\boldsymbol{H}]\!]) \bullet \delta\boldsymbol{A}_t$.

divergence theorem gives the stationary condition

$$\mathscr{F}_{,\boldsymbol{u}}[\delta\boldsymbol{u}] = \int_{t^1}^{t^2}\left\{\int_{\mathbb{R}^3}\left(\boldsymbol{\nabla}\bullet\boldsymbol{\Pi} - \frac{\mathrm{d}}{\mathrm{d}t}(((\varepsilon_0 J\tilde{\boldsymbol{E}}\bullet\boldsymbol{C}^{-1})\times\boldsymbol{B})\bullet\boldsymbol{F}^{-1}) - \rho_0\ddot{\boldsymbol{u}} + \rho_0\boldsymbol{f}\right)\bullet\delta\boldsymbol{u}\,\mathrm{d}V - \int_{\partial\Omega}(\boldsymbol{N}\bullet[\![\boldsymbol{\Pi}]\!] - \boldsymbol{T})\bullet\delta\boldsymbol{u}\,\mathrm{d}S\right\}\mathrm{d}t = 0, \tag{2.69}$$

where the reference electromagnetic–mechanical first Piola–Kirchhoff stress $\boldsymbol{\Pi}$ is given by

$$\boldsymbol{\Pi} = \rho_0\left(\frac{\partial\psi}{\partial\boldsymbol{F}}\right)^T + \varepsilon_0 J\left((\tilde{\boldsymbol{E}}\bullet\boldsymbol{C}^{-1})(\boldsymbol{C}^{-1}\bullet\tilde{\boldsymbol{E}})\bullet\boldsymbol{F}^T - \frac{1}{2}(\tilde{\boldsymbol{E}}\bullet\boldsymbol{C}^{-1}\bullet\tilde{\boldsymbol{E}})\boldsymbol{F}^{-1}\right) + \frac{1}{\mu_0 J}\left(\boldsymbol{B}\boldsymbol{B}\bullet\boldsymbol{F}^T - \frac{1}{2}(\boldsymbol{B}\bullet\boldsymbol{C}\bullet\boldsymbol{B})\boldsymbol{F}^{-1}\right) + (\boldsymbol{F}^{-1}\bullet\dot{\boldsymbol{u}})(\boldsymbol{D}\times\boldsymbol{B})\bullet\boldsymbol{F}^{-1}. \tag{2.70}$$

Consequently from Eqs. (2.69) and (2.70) one obtains

$$\boldsymbol{\nabla}\bullet\boldsymbol{\Pi} + \rho_0\boldsymbol{f} = \frac{\mathrm{d}}{\mathrm{d}t}((\boldsymbol{D}\times\boldsymbol{B})\bullet\boldsymbol{F}^{-1}) + \rho_0\ddot{\boldsymbol{u}} = \rho_0\dot{\boldsymbol{g}}, \quad \boldsymbol{N}\bullet[\![\boldsymbol{\Pi}]\!] = \boldsymbol{T}, \tag{2.71}$$

which are the reference configuration equation of motion and interface condition of Eq. (2.55) as expected.

A final note is in order at this point. To complete the variational formulation presentation one must show that Eq. (2.71) transforms to its current configuration counterpart. Using the $\boldsymbol{\sigma}$–$\boldsymbol{\Pi}$ relation in Eq. (2.54) one has

$$\boldsymbol{\nabla}\bullet\boldsymbol{\Pi} = J(\nabla\bullet\boldsymbol{\sigma}). \tag{2.72}$$

Considering in addition Eqs. (2.5), (2.25), (2.37), (2.39), (2.42), (2.51), and (2.60), the reference configuration equation and interface conditions of motion transform to Eq. (2.35) and the interface condition in Eq. (2.18), their current configuration counterparts derived with the direct method. It is thus shown that the variational method agrees with the direct method for Maxwell's equations and the equation of motion.

3. Eddy current formulation

For the EMF processes of interest the problem formulation may be simplified considerably by applying the eddy current approximation. Following the description of the eddy current approximation for the general 3-D case, the section proceeds with the axisymmetric version of this approximation and ends by presenting the modeling of the coil under a given current.

3.1. General case in 3-D

The aspects typical of EMF processes that make this simplification appropriate are: the material velocities are much less than the speed of light, the effective electric current frequencies are on the order of 10 kHz, the geometry is on the order of 1 mm, and the material electrical conductivities are large. Detailed discussion of this approximate formulation may be found in the literature, e.g. in Hiptmair and Ostrowski (2005) and references cited therein. From the above assumptions follows that the eddy current approximation essentially consists of neglecting electric energy from the Lagrangian ℓ in Eq. (2.57). Imposing the eddy current approximation implies displacement currents are neglected, which means volumetric charges are not accounted for and charge conservation must be imposed separately. The resulting approximate Lagrangian does not depend on Φ and Gauss' equation is no longer a result of the variational procedure.

With this approximation, the Lagrangian may be divided into kinetic energy, $\mathscr{K}$, and potential energy, $\mathscr{P}$, as

$$\mathscr{L} \equiv \mathscr{K} - \mathscr{P}, \tag{3.1}$$

where $\mathscr{K}$ and $\mathscr{P}$ are given by

$$\mathscr{K} \equiv \int_{\mathbb{R}^3}\frac{\rho_0}{2}(\dot{\boldsymbol{u}}\bullet\dot{\boldsymbol{u}})\,\mathrm{d}V,$$
$$\mathscr{P} \equiv \int_{\mathbb{R}^3}\left(\frac{1}{2\mu_0 J}(\boldsymbol{B}\bullet\boldsymbol{C}\bullet\boldsymbol{B}) - \boldsymbol{J}\bullet\boldsymbol{A} + \rho_0(\psi - \boldsymbol{f}\bullet\boldsymbol{u})\right)\mathrm{d}V - \int_{\partial\Omega}\boldsymbol{T}\bullet\boldsymbol{u}\,\mathrm{d}S. \tag{3.2}$$

The action integral $\mathscr{F}$ is formed by integrating $\mathscr{L}$ over a time interval $[t^1, t^2]$, and Hamilton's principle is applied as previously (see Eq. (2.62)). Taking the variation of $\mathscr{F}$ with respect to $\boldsymbol{A}$ gives

$$\mathscr{F}_{,\boldsymbol{A}}[\delta\boldsymbol{A}] = \int_{t^1}^{t^2}\left\{\int_{\mathbb{R}^3}\left(-\boldsymbol{\nabla}\times\left(\frac{1}{\mu_0 J}(\boldsymbol{B}\bullet\boldsymbol{C})\right) + \boldsymbol{J}\right)\bullet\delta\boldsymbol{A}\,\mathrm{d}V - \int_{\partial\Omega}[\![\left(\boldsymbol{N}\times\left(\frac{1}{\mu_0 J}(\boldsymbol{B}\bullet\boldsymbol{C})\right)\right)\bullet\delta\boldsymbol{A}]\!]\mathrm{d}S\right\}\mathrm{d}t = 0. \tag{3.3}$$

The eddy current simplification implies that the terms in parentheses in Eq. (3.3) are the reference configuration H field. From Eq. (2.67) and since $\mu_0\varepsilon_0 \ll 1$ one can define the approximate H field by

$$\boldsymbol{H} \equiv \frac{1}{\mu_0 J}(\boldsymbol{B} \bullet \boldsymbol{C}). \tag{3.4}$$

Thus the variation with respect to $\boldsymbol{A}$ results in the reference configuration approximate Ampere's equation and interface condition, given by

$$\boldsymbol{\nabla} \times \boldsymbol{H} = \boldsymbol{J}, \quad \boldsymbol{N} \times [\![\boldsymbol{H}]\!] = \boldsymbol{0}, \tag{3.5}$$

which agrees with Eq. (2.68) once the displacement current $\dot{\boldsymbol{D}}$ is neglected.

Taking the variation of $\mathscr{F}$ with respect to $\boldsymbol{u}$, one has

$$\mathscr{F}_{,\boldsymbol{u}}[\delta \boldsymbol{u}] = \int_{t^1}^{t^2} \left\{ \int_{\mathbb{R}^3} (\boldsymbol{\nabla} \bullet \boldsymbol{\Pi} - \rho_0 \ddot{\boldsymbol{u}} + \rho_0 \boldsymbol{f}) \bullet \delta \boldsymbol{u} \, \mathrm{d}V - \int_{\partial\Omega} (\boldsymbol{N} \bullet [\![\boldsymbol{\Pi}]\!] - \boldsymbol{T}) \bullet \delta \boldsymbol{u} \, \mathrm{d}S \right\} \mathrm{d}t = 0, \tag{3.6}$$

where the approximate nominal stress field $\boldsymbol{\Pi}$ has now been defined as

$$\boldsymbol{\Pi} \equiv \rho_0 \left(\frac{\partial \psi}{\partial \boldsymbol{F}} \right)^T + \frac{1}{\mu_0 J} \left(\boldsymbol{B}\boldsymbol{B} \bullet \boldsymbol{F}^T - \frac{1}{2} (\boldsymbol{B} \bullet \boldsymbol{C} \bullet \boldsymbol{B}) \boldsymbol{F}^{-1} \right). \tag{3.7}$$

Eq. (3.6) implies the pointwise equation of motion and interface condition in the reference configuration,

$$\boldsymbol{\nabla} \bullet \boldsymbol{\Pi} + \rho_0 \boldsymbol{f} = \rho_0 \ddot{\boldsymbol{u}}, \quad \boldsymbol{N} \bullet [\![\boldsymbol{\Pi}]\!] = \boldsymbol{T}, \tag{3.8}$$

which results from Eq. (2.71) when electric displacement terms are neglected.

To complete the formulation, charge conservation must be imposed separately, since it cannot follow from Hamilton's principle with the eddy current simplification. The reference configuration charge conservation equation and interface condition are

$$\boldsymbol{\nabla} \bullet \boldsymbol{J} = 0, \quad \boldsymbol{N} \bullet [\![\boldsymbol{J}]\!] = 0 \tag{3.9}$$

and must be imposed in addition to Hamilton's principle for the eddy current approximation.

To solve the governing equations (3.5), (3.8), and (3.9), the constitutive law for $\boldsymbol{J}$ is needed. Here we assume an isotropic Ohm's law with constant conductivity, given by

$$\boldsymbol{j} = \sigma(\boldsymbol{e} + \dot{\boldsymbol{u}} \times \boldsymbol{b}) \;\Rightarrow\; \boldsymbol{J} = \sigma J \boldsymbol{C}^{-1} \bullet \boldsymbol{E}. \tag{3.10}$$

In addition, since ψ may depend also on internal variables $\boldsymbol{\xi}$, an evolution law of the type—typical for theories of metal plasticity—$\dot{\boldsymbol{\xi}} = \boldsymbol{\Xi}(\boldsymbol{\sigma}, T, \boldsymbol{\xi})$ might also be needed.

3.2. Axisymmetric processes

Implementing the aforementioned general theoretical formulation for axisymmetric problems significantly simplifies the formulation (given subsequently in cylindrical coordinates) by reducing the independent variables on the (R, Z) space to three (A_Θ, u_R, u_Z), as it will be shown in the first subsection.[14] However, special care must be taken with the axisymmetric formulation in the forming coil under a given current, and this is the object of the second subsection.

3.2.1. Axisymmetric formulation

The forming process of interest is assumed rotationally symmetric (in the z-direction), implying that no field depends on the θ coordinate. The corresponding symmetry group is C_∞, i.e. when the solution is invariant to coordinate transformations corresponding to solid body rotations around the z-axis. From the assumed symmetry it is expected that there is no hoop displacement ($u_\theta = 0$) and the only non-zero component of the current density and electric field is the hoop component, i.e. $\boldsymbol{j} = j_\theta \boldsymbol{i}_\theta$ and $\boldsymbol{e} = e_\theta \boldsymbol{i}_\theta$. Also from symmetry, there is no hoop component of the magnetic field ($\boldsymbol{b}_\theta = 0$). To summarize,

$$\begin{aligned} &\frac{\partial ()}{\partial \theta} = 0; \quad u_r, u_z \neq 0, \quad u_\theta = 0; \quad e_r, e_z = 0, \quad e_\theta \neq 0; \\ &b_r, b_z \neq 0, \quad b_\theta = 0; \quad j_r, j_z = 0, \quad j_\theta \neq 0. \end{aligned} \tag{3.11}$$

[14] Here and subsequently r, θ, and z are current configuration cylindrical coordinates with respective cylindrical unit vectors $\boldsymbol{i}_r$, $\boldsymbol{i}_\theta$, and $\boldsymbol{i}_z$, and R, Θ, and Z are reference configuration cylindrical coordinates with respective cylindrical unit vectors $\boldsymbol{i}_R$, $\boldsymbol{i}_\Theta$, $\boldsymbol{i}_Z$. For the case currently of interest $r = R + u_R$, $\theta = \Theta$, and $z = Z + u_Z$, and therefore $\boldsymbol{i}_r = \boldsymbol{i}_R$, $\boldsymbol{i}_\theta = \boldsymbol{i}_\Theta$, and $\boldsymbol{i}_z = \boldsymbol{i}_Z$.

The above results are consistent with Ohm's law, Eq. (3.10). Moreover from the electric field-potential relation, Eq. (2.56), combined with Eq. (3.11), one obtains that

$$a_r, a_z = 0, \quad a_\theta \neq 0; \quad \frac{\partial \phi}{\partial r} = \frac{\partial \phi}{\partial z} = \frac{\partial \phi}{\partial \theta} = 0, \tag{3.12}$$

i.e. the only independent fields are a_θ, u_r, and u_z. Using the relations between current and reference configuration electric current and potentials, Eqs. (2.47) and (2.59) respectively, one has in the reference configuration

$$\boldsymbol{u} = u_R \boldsymbol{i}_R + u_Z \boldsymbol{i}_Z, \quad \boldsymbol{A} = A_\Theta \boldsymbol{i}_\Theta, \quad \Phi = 0, \quad \boldsymbol{J} = J_\Theta \boldsymbol{i}_\Theta, \tag{3.13}$$

where Φ may be chosen as any arbitrary constant and is here set to zero.

With this formulation in place, it is straightforward to show that the Coulomb gauge condition, charge conservation, and two associated interface conditions in the reference configuration are identically satisfied, that is

$$\begin{aligned} &\boldsymbol{\nabla} \bullet \boldsymbol{A} = 0, \\ &\boldsymbol{N} \bullet [\![\boldsymbol{A}]\!] = 0, \\ &\boldsymbol{\nabla} \bullet \boldsymbol{J} = 0, \\ &\boldsymbol{N} \bullet [\![\boldsymbol{J}]\!] = 0. \end{aligned} \tag{3.14}$$

Note that, whereas Eqs. $(3.14)_3$ and $(3.14)_4$ must hold in 3-D processes as well, Eqs. $(3.14)_1$ and $(3.14)_2$ are here a result of axisymmetry. In general, other gauge conditions may be chosen, and non-zero jumps in the normal of the vector potential may occur.

Axisymmetric processes may include applied mechanical body forces $\boldsymbol{f}$ and surface tractions $\boldsymbol{T}$, but neither is needed in the subsequent free electromagnetic tube expansion simulations. The applied mechanical body force $\boldsymbol{f}$ may be ignored since gravity is weak compared to the electromagnetic forces, and there is no applied mechanical surface traction $\boldsymbol{T}$ since the processes are non-contact. Thus, here and subsequently $\boldsymbol{f}$ and $\boldsymbol{T}$ are set to zero.

3.2.2. Forming coil

Though the forming process of interest is assumed to be geometrically axisymmetric, the forming coil in reality must be a continuous spiral. In order to model such a coil in the axisymmetric framework, the formulation must include the driving electric field. The approach here is similar to that in Stiemer et al. (2006). Each coil turn is approximated as a stationary torus, disconnected geometrically from the other turns. It is required that the electric current density remain axisymmetric, which implies in each coil turn

$$\boldsymbol{J} = J_\Theta(R, Z) \boldsymbol{i}_\Theta. \tag{3.15}$$

Using Eqs. (2.58) and (3.10) and recalling that the coil does not deform (reference and current configuration are the same), one has

$$\begin{aligned} &J_R = 0 \;\Rightarrow\; \frac{\partial \Phi}{\partial R} = A_R = 0, \\ &J_Z = 0 \;\Rightarrow\; \frac{\partial \Phi}{\partial Z} = A_Z = 0. \end{aligned} \tag{3.16}$$

Thus Φ is not a function of R or Z, and from Eq. (3.15) J_Θ is not a function of Θ. Since $J_\Theta = -\sigma((1/R)\partial\Phi/\partial\Theta + \dot{A}_\Theta)$, $\partial\Phi/\partial\Theta$ must in view of Eq. (3.16) be a constant. Given ΔU_k, the change in the electric potential Φ over coil turn k,

$$\frac{\partial \Phi}{\partial \Theta} = \frac{\Delta U_k}{2\pi} \;\Rightarrow\; \boldsymbol{\nabla}\Phi = \left(\frac{\Delta U_k}{2\pi R}\right) \boldsymbol{i}_\Theta. \tag{3.17}$$

With this formulation, the electric potential drop in turn k, ΔU_k, can be expressed in terms of the coil current $I(t)$ and the magnetic vector potential A_Θ as follows: Recall from Ohm's law, Eq. (3.10), that since the coil does not deform, $\boldsymbol{J} = \boldsymbol{j} = \sigma \boldsymbol{e} = \sigma \boldsymbol{E}$. Integrating over the cross-section in the R–Z plane of a coil turn gives the total current in the coil, $I(t)$. Assuming the coil has a rectangular cross-section in the R–Z plane aligned with the R–Z-axes

$$\begin{aligned} I(t) &= \int_{S_k} \boldsymbol{J} \bullet \boldsymbol{n}_k \, \mathrm{d}S \\ &= -\sigma \int_{S_k} (\boldsymbol{\nabla}\Phi + \dot{\boldsymbol{A}}) \bullet \boldsymbol{i}_\Theta \, \mathrm{d}S \\ &= -\sigma \int_{S_k} \left(\dot{A}_\Theta + \frac{\Delta U_k}{2\pi R}\right) \mathrm{d}S \\ &= -\sigma \int_{S_k} \dot{A}_\Theta \mathrm{d}S - \frac{\sigma h_k}{2\pi} \ln\left(\frac{b_k}{a_k}\right) \Delta U_k, \end{aligned} \tag{3.18}$$

where S_k is the surface of the coil's cross-section in the R–Z plane, $\boldsymbol{n}_k = \boldsymbol{i}_\Theta$ is the normal to the cross-section, h_k is the height of the cross-section, b_k is the outside radius of the cross-section, and a_k is the inside radius of the cross-section. This equation may be solved for ΔU_k in terms of $I(t)$ and $\dot{A}_\Theta$, and using in addition Eqs. (2.58), (3.10), and (3.17) the hoop

component electric current density in coil turn k is given by

$$J_\Theta = \frac{\sigma}{h_k R}\left(\ln\left(\frac{b_k}{a_k}\right)\right)^{-1}\left(\frac{I(t)}{\sigma}+\int_{S_k}\dot{A}_\Theta\,\mathrm{d}S\right)-\sigma\dot{A}_\Theta. \tag{3.19}$$

This expression for the electric current density in the coil is substituted into the variational formulation, Eq. (3.2), to yield a boundary value problem dependent only on A_Θ.

4. Numerical implementation

The numerical implementation of the general theory employs the variational integration approach. According to this method, space and time interpolation schemes are concurrently applied to the Lagrangian, followed by the variational principle applied on the discrete nodal variables for each time step. A survey of the extensive literature on this topic may be found in the introductory discussion of Marsden and West (2001).

In the axisymmetric cases discussed here, the independent variables, functions of R and Z, are: non-zero magnetic vector potential component A_Θ and non-zero displacement components u_R and u_Z. All the independent variables are continuous functions of the space variables, as discussed in Section 3.2. Therefore, employing nodal finite elements one has the discretization in space, given by

$$\begin{aligned}&\boldsymbol{A}_e(R,Z;t)\approx\boldsymbol{M}(R,Z)\bullet\boldsymbol{q}_e(t),\\&\boldsymbol{u}_e(R,Z;t)\approx\boldsymbol{N}(R,Z)\bullet\boldsymbol{p}_e(t),\end{aligned} \tag{4.1}$$

where $\boldsymbol{A}_e$ is the vector potential $\boldsymbol{A}$ inside an element, $\boldsymbol{M}$ is the spatial interpolation matrix of element basis functions for $\boldsymbol{A}_e$, $\boldsymbol{q}_e$ are the nodal degrees of freedom for $\boldsymbol{A}_e$, $\boldsymbol{u}_e$ is the displacement $\boldsymbol{u}$ inside an element, $\boldsymbol{N}$ is the spatial interpolation matrix of element basis functions for $\boldsymbol{u}_e$, and $\boldsymbol{p}_e$ are the nodal degrees of freedom for $\boldsymbol{u}_e$. Four node bilinear quadrilateral elements are used to discretize $\boldsymbol{A}$ and $\boldsymbol{u}$, with the same mesh being employed for each variable. These linear elements are appropriate since the Lagrangian, Eq. (3.1), involves only up to first derivatives of continuous functions $\boldsymbol{A}$ and $\boldsymbol{u}$.

Using the backward Euler approximation for time discretization, one has

$$\begin{aligned}&\dot{\boldsymbol{A}}_e(R,Z;t^i)\approx\boldsymbol{M}(R,Z)\bullet\dot{\boldsymbol{q}}_e(t^i),\quad \dot{\boldsymbol{q}}_e(t^i)\approx\frac{\boldsymbol{q}_e^i-\boldsymbol{q}_e^{i-1}}{\Delta t},\\&\dot{\boldsymbol{u}}_e(R,Z;t^i)\approx\boldsymbol{N}(R,Z)\bullet\dot{\boldsymbol{p}}_e(t^i),\quad \dot{\boldsymbol{p}}_e(t^i)\approx\frac{\boldsymbol{p}_e^i-\boldsymbol{p}_e^{i-1}}{\Delta t},\end{aligned} \tag{4.2}$$

where $\boldsymbol{q}_e^i$ and $\boldsymbol{p}_e^i$ are the degrees of freedom in an element at time t^i and where the time step $\Delta t\equiv t^i-t^{i-1}$. With the above space and time discretization and using the right-hand rule for time integration of $\mathscr{F}$, a discrete action $\mathscr{F}^d$ is defined by

$$\begin{aligned}\mathscr{F}&\equiv\int_{t^0}^{t^M}\mathscr{L}(\boldsymbol{A},\boldsymbol{u},\dot{\boldsymbol{u}})\,\mathrm{d}t\\&\approx\Delta t\sum_{i=1}^{M}\mathscr{L}_i^d(\boldsymbol{q}^i,\boldsymbol{p}^{i-1},\boldsymbol{p}^i)\equiv\mathscr{F}^d,\end{aligned} \tag{4.3}$$

where the Lagrangian is given in Eq. (3.1) and its discrete approximation at time t^i, $\mathscr{L}_i^d(\boldsymbol{q}^i,\boldsymbol{p}^{i-1},\boldsymbol{p}^i)$, follows from applying the discretization equations (4.1) and (4.2). Also, $\boldsymbol{q}^i$ and $\boldsymbol{p}^i$ are the degrees of freedom at time t^i throughout the space domain. Upon application of Hamilton's variational principle with respect to these discrete degrees of freedom, the discrete governing equations are

$$\mathscr{F}^d_{,\boldsymbol{q}^i}[\delta\boldsymbol{q}^i]=0,\quad \mathscr{F}^d_{,\boldsymbol{p}^i}[\delta\boldsymbol{p}^i]=0, \tag{4.4}$$

where $\delta\boldsymbol{q}^0=\delta\boldsymbol{q}^M=\boldsymbol{0}$ and $\delta\boldsymbol{p}^0=\delta\boldsymbol{p}^M=\boldsymbol{0}$. These equations provide the time stepping routine to solve for the degrees of freedom at each time step, i.e. given $[\boldsymbol{q}^i,\boldsymbol{q}^{i-1},\boldsymbol{p}^i,\boldsymbol{p}^{i-1}]$ one calculates $[\boldsymbol{q}^{i+1},\boldsymbol{p}^{i+1}]$. The choice of the approximations to the time derivatives and integral in Eqs. (4.2) and (4.3), respectively, results in implicit time integration for $\boldsymbol{q}$ and explicit time integration for $\boldsymbol{p}$.

That is, at each time step the finite element problem is

$$\begin{aligned}&\boldsymbol{K}(\boldsymbol{p}^{i+1})\bullet\boldsymbol{q}^{i+1}=\boldsymbol{f}_q(\boldsymbol{q}^i,\boldsymbol{p}^{i+1};t^{i+1}),\\&\boldsymbol{R}\bullet\boldsymbol{p}^{i+1}=\boldsymbol{f}_p(\boldsymbol{q}^i,\boldsymbol{p}^{i-1},\boldsymbol{p}^i)\ \Rightarrow\ \boldsymbol{p}^{i+1}=\boldsymbol{R}^{-1}\bullet\boldsymbol{f}_p,\end{aligned} \tag{4.5}$$

where $\boldsymbol{K}$ is the tangent matrix associated with the electromagnetic degrees of freedom, $\boldsymbol{f}_q$ is the force vector associated with the electromagnetic degrees of freedom, $\boldsymbol{R}$ is the constant mass matrix associated with the mechanical degrees of freedom, and $\boldsymbol{f}_p$ is the force vector associated with the mechanical degrees of freedom. One may calculate nodal displacements $\boldsymbol{p}^{i+1}$ from Eq. $(4.5)_2$ where the mass matrix $\boldsymbol{R}$ is constant. Then the nodal vector potential $\boldsymbol{q}^{i+1}$ is given in terms of $\boldsymbol{q}^i$ and $\boldsymbol{p}^{i+1}$ by Eq. $(4.5)_1$ where the tangent matrix $\boldsymbol{K}(\boldsymbol{p}^{i+1})$ depends on the current geometry. Notice that the resulting scheme is an efficient staggered solution algorithm with two uncoupled solution steps, neither of which requires an iterative solution technique.

To complete the implementation the initial and boundary conditions are needed. The initial conditions are given by

$$\boldsymbol{A} = \boldsymbol{0}, \quad \boldsymbol{u} = \boldsymbol{0}, \quad \dot{\boldsymbol{u}} = \boldsymbol{0} \text{ at } t = 0. \tag{4.6}$$

Note that the problem is driven by the time dependent input electric current $I(t)$, as discussed in Section 3.2.2.

The problem also requires application of the essential boundary conditions. In addition to axisymmetry, the processes modeled subsequently will all have mirror symmetry around $Z = 0$. This implies the essential boundary conditions for $\boldsymbol{A}$ are

$$\begin{aligned} &A_\Theta = 0 \quad \text{at } R = 0, \\ &A_\Theta \to 0 \quad \text{as } R^2 + Z^2 \to \infty. \end{aligned} \tag{4.7}$$

$R = 0$ is the axis of rotational symmetry, implying $A_\Theta = 0$, and the electromagnetic fields decay to zero at infinity. For simplicity, the latter boundary condition is implemented by taking a large area of meshed air and applying $A_\Theta = 0$ at the edges. In the following calculations it has been confirmed that the size of the air mesh is large enough as to accurately model the infinity boundary condition. For $\boldsymbol{u}$, we need to impose only the boundary condition

$$u_Z = 0 \quad \text{at} \quad Z = 0, \tag{4.8}$$

which is dictated by mirror symmetry about $Z = 0$.

Note that outside the workpiece the displacements are not determined by the variational procedure. The coil is stationary, and in the surrounding air the equation of motion is satisfied identically, as expected. However, it is necessary to assume a kinematically admissible displacement field in the air in order to ensure the mapping between reference and current configurations remains invertible, i.e. a non-singular $\boldsymbol{K}(\boldsymbol{p}^{i+1})$ in Eq. (4.5). Moreover, this distribution affects the numerical solution and if not carefully chosen can cause the simulation to give poor results. In the present work, a simple linear distribution of displacements in the air is implemented that adjusts with the displacements in the workpiece as necessary.

It is also important to note the influence of the forming coil on the finite element matrices. Eq. (3.19) implies that each degree of freedom in a coil turn cross-section is directly coupled to every other one, through the integral over the cross-section. This introduces non-local relations into the finite element method, and the resulting tangent matrix $\boldsymbol{K}$ in Eq. (4.5) is asymmetric.

In the most general case ψ also depends on internal variables ξ. Accordingly, evolution laws for $\dot{\xi}$ must also be included into the numerical algorithm. The constitutive law adopted for the metallic tubes simulated here is for simplicity a deformation theory of plasticity with unloading, which could be cast as a one internal variable model. Due to the relative simplicity of this model, the numerical algorithm does not need an internal variable evolution law, as it is detailed in the Appendix.

The numerical techniques detailed above are implemented using the finite element program FEAP (2005). Moreover, the choice of the numerical integration techniques will be discussed further in a subsequent publication, where details of the solution algorithm will be given, along with an analysis of the technique and possible alternatives.

5. Simulation results

The ensuing simulations of electromagnetically driven, freely expanding tubes are inspired by the experimental work of Seth (2006). These experiments addressed the onset of necking in freely expanding, electromagnetically loaded tubes, and their localization of deformation aspects were modeled by Thomas et al. (2007). Given that the expanded tubes remained mostly axisymmetric in these experiments, we will use the geometries, material properties, and currents of some of these experiments for the calculations in this work. In the following simulations, a cylindrical four turn coil expands three tubes of varying height: one taller than the coil, one of approximately even height with the coil (denoted as "intermediate"), and one shorter than the coil. Moreover, motivated by the work of Zhang and Ravi-Chandar (2008a) on the influence of coatings on the ductility of tubes under high strain rates, the expansion of the tall tube externally coated by a non-conductive hyperelastic material is also analyzed.

The geometry of the tube expansion setup is shown in Fig. 1a, where the coil is idealized as axisymmetric rings. Fig. 1b shows the simulation domain (top right quarter of the plane $\Theta = 0$) with the relevant dimensions. The midlines of the coil turns and tube are denoted with solid dots, and the midplane of the tube is denoted with a dashed line. The relevant dimensions are: radius of the coil midlines, R_c; radius of tube midline, R_t; pitch of the coil, P_c; one-half height of the tube, Z_t; coil turn cross-section thickness, T_c; tube cross-section thickness, T_t; and hyperelastic coating cross-section thickness, T_h. Note that the coil dimensions from Section 3.2.2 are thus $h_k = T_c$, $a_k = R_c - T_c/2$, and $b_k = R_c + T_c/2$.

This section starts with a presentation of the meshing and time steps, followed by the choice of constitutive properties and proceeds with the simulation results.

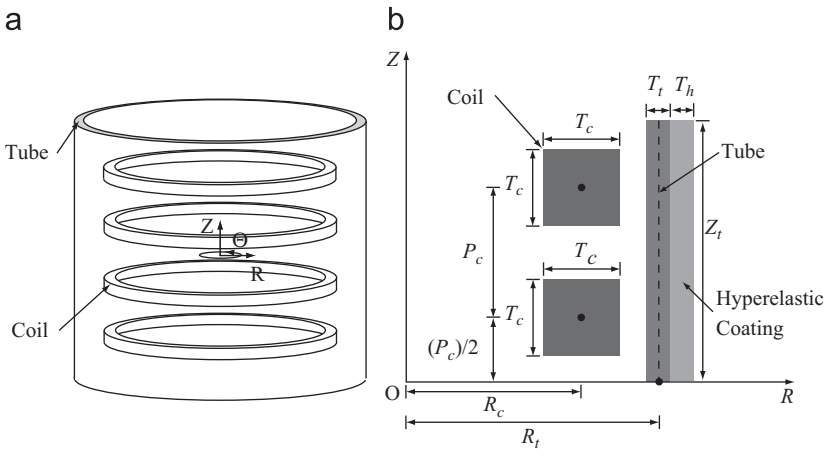

Fig. 1. (a) Idealized tube expansion setup. (b) Simulation domain and dimensions.

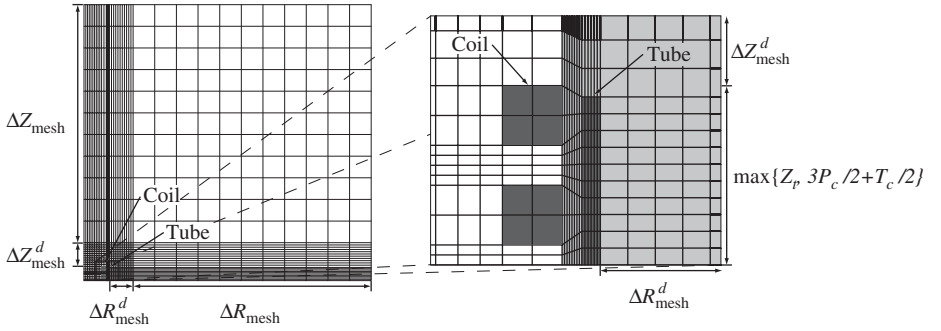

Fig. 2. Example FEM mesh for axisymmetric tube expansion.

5.1. Meshing and time steps

The reference configuration finite element meshes are for simplicity distorted Cartesian grids. As a check, the mesh density employed was shown to give, during the duration of the simulation, a maximum midline displacement for the tall tube less than 1% different than a mesh four times denser. Fig. 2 is an FEM mesh of the intermediate tube. The tube and coil are depicted in dark gray, and the air is depicted in white and light gray. Throughout the following calculations we use the same basic mesh, with adjustments to accommodate changes in tube geometry, that has four elements in each square coil turn, approximately 700 elements in the tall tube, and the same density of elements in the coatings as in the tubes. The result is 5000–10,000 nodes in each problem.

There are two regions of air mesh: one that moves during the process with assigned displacements (necessary near the tube, see Section 4) and one fixed. The air region in light gray in Fig. 2 has displacements that vary linearly from the tube surface to the boundary of the region. This region covers, in the R direction, from the outside radius of the coil ($R = R_c + T_c/2$) to a distance ΔR^d_{mesh} beyond the outside of the tube and, in the Z direction, from $Z = 0$ to a distance ΔZ^d_{mesh} beyond the top of the coil or tube, whichever is taller. The remaining air in the simulation domain (white in Fig. 2) is fixed, and the simulation domain extends beyond the region with non-zero air displacements distances of ΔR_{mesh} and ΔZ_{mesh} in the R and Z directions, respectively. These dimensions, which are labeled in Fig. 2, are chosen relative to the inner radius of the tube, $R_t^{\text{in}} = R_t - T_t/2$. Based on convergence studies, all the subsequent simulations use $\Delta R^d_{\text{mesh}} = \Delta Z^d_{\text{mesh}} = R_t^{\text{in}}$ and $\Delta R_{\text{mesh}} = \Delta Z_{\text{mesh}} = 10R_t^{\text{in}}$.

The time step Δt is chosen for stability and accuracy, which are affected by the elastic wave speed (and thus the size of the elements in solids) and characteristic time of the electric current pulse. The need to resolve elastic waves is the limiting factor, and since the mesh and problem geometry are similar in each of the following simulations, the time step is kept constant throughout the following work. The characteristic time of the electric current pulse, where t_0 will be one-half the pulse time, controls the macroscopic deformation, and for the values of t_0 in this work we have $\Delta t/t_0 = 3 \times 10^{-4}$ or less. In general, decreasing the time step below the value we use showed negligible change in the solution. The influence of mesh and time step will be discussed in detail in a subsequent publication.

Table 1
Electromagnetic constitutive parameter values.

$\mu_0 = 1.26 \times 10^{-6}\,\mathrm{N/A^2}$	$\varepsilon_0 = 8.85 \times 10^{-12}\,\mathrm{F/m}$	$r_{Al} = 2.65 \times 10^{-8}\,\Omega\,\mathrm{m}$	$r_{Cu} = 1.68 \times 10^{-8}\,\Omega\,\mathrm{m}$

Table 2
AA6063-T6 uniaxial mechanical constitutive parameter values.

$E = 69 \times 10^9\,\mathrm{Pa}$	$\tau_y = 195 \times 10^6\,\mathrm{Pa}$	$m = 13.89$	$\nu = 0.33$	$\rho_0 = 2700\,\mathrm{kg/m^3}$

5.2. Material constitutive behavior

In the interest of simplicity temperature effects are ignored. The corresponding electromagnetic and mechanical material response models adopted are discussed below.

5.2.1. Electromagnetic constitutive response

Since the applications of interest involve metals under high current density, magnetization and polarization can be safely ignored, and Eq. (2.25) gives the constitutive relations between the magnetic field and H field and between the electric field and electric displacement. In addition, Ohm's law is required to relate electric current density with electric field, and its constant conductivity version is given in Eq. (3.10). The resistivity of aluminum, r_{Al} (the experimental tubes were made of AA6063-T6 aluminum alloy), and copper, r_{Cu} (typical actuators are made of copper), have been obtained from standard tables. Also, note that the coatings applied to the tall tube are assumed to have zero conductivity. The values of the electromagnetic constitutive parameters (which in addition to the resistivities include μ_0 and ε_0 the permeability and permittivity of vacuum) are given in Table 1.

5.2.2. Mechanical constitutive response

The constitutive law employed for the tubes is a finite strain model extension of J_2 deformation theory of plasticity (a generalization of the model employed by Abeyaratne and Triantafyllidis (1981), and see the references cited therein for more details). For metals undergoing moderate deformations with nearly proportional loading, the J_2 deformation theory of plasticity model has been shown to give reasonable experimental predictions (Anand, 1979). A useful feature of this formulation is that it can be fit to any uniaxial stress–strain response. Because of this feature, this formulation can also be used to model the polyurea coating of interest in Zhang and Ravi-Chandar (2008a), which is approximated as an isotropic hyperelastic solid. For comparison purposes a compressible Mooney–Rivlin model (Hallquist, 2006) is also used as an alternative coating on the tall tube. For completeness these two constitutive models may be found in the Appendix.

The experimentally obtained quasistatic uniaxial response for the tube alloy AA6063-T6 has been fitted to a piecewise power law. The resulting Young's modulus E, yield stress τ_y, and hardening exponent m are given in Table 2. A comparison of the uniaxial stress–strain data and the piecewise power law fit is shown in Fig. 3. Poisson's ratio ν and the reference configuration mass density ρ_0 also shown in Table 2 are obtained from standard tables on aluminum (they are not alloy sensitive).

A similar procedure has been followed to obtain the piecewise power law fit parameters for the polyurea coating used in the experiments of Zhang and Ravi-Chandar (2008a) (for uniaxial data see the cast polyurea material of Chakkarapani et al., 2006). Poisson's ratio is chosen such that the material is close to incompressible while also avoiding numerical difficulties, and the mass density was obtained from Zhang and Ravi-Chandar (2008a). The resulting material parameters are given in Table 3.

A comparison of the uniaxial stress–strain data and the piecewise power law fit is shown in Fig. 4. On the same figure is plotted the uniaxial stress–strain response of a Mooney–Rivlin coating with the same Young's modulus E and Poisson's ratio ν.

All the ingredients are now in place to proceed with the simulations of electromagnetically expanded tubes.

5.3. Tube expansion

The geometry of the four different tube expansion simulations (three uncoated and one coated tube) is given in Table 4. Each coil turn has a square cross-section with the same area as the circular cross-sections of the coils in the experiments of Seth (2006) (square-cross-sections simplify meshing of the coil). Also, the height of the short tube is two thirds that of the intermediate tube (the short tube case is not based on an experiment), and the coated tubes are simply the tall tube with coating applied to the outside surface.

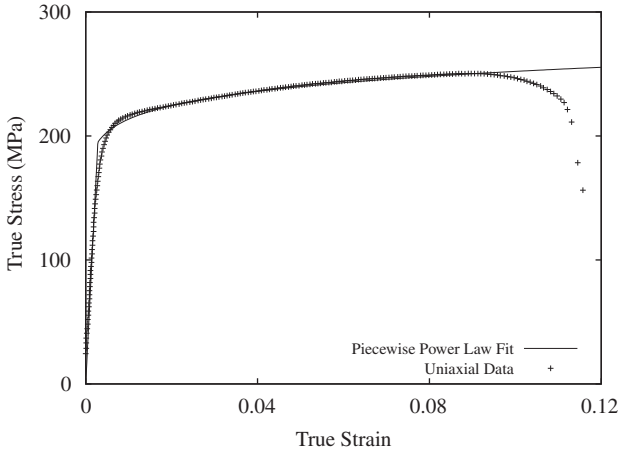

Fig. 3. Comparison of experimental data and piecewise power law fit for AA6063-T6.

Table 3
Polyurea uniaxial mechanical constitutive parameter values.

$E = 73 \times 10^6$ Pa	$\tau_y = 3.8 \times 10^6$ Pa	$m = 2.817$	$\nu = 0.45$	$\rho_0 = 1200\,\mathrm{kg/m^3}$

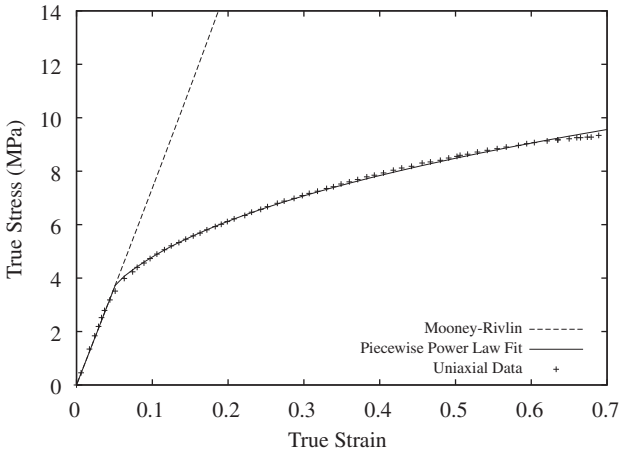

Fig. 4. Comparison of experimental data and piecewise power law fit for polyurea coatings. The response of a Mooney–Rivlin coating with the same Young's modulus E and Poisson's ratio ν is also plotted.

Table 4
Geometry of tube expansion simulations.

	Tall tube (m)	Intermediate tube (m)	Short tube (m)	Coated tall tubes (m)
R_c	0.023825	0.023825	0.023825	0.023825
R_t	0.029375	0.029375	0.029375	0.029375
P_c	0.0094	0.0094	0.0094	0.0094
Z_t	0.04255	0.01585	0.01057	0.04255
T_c	0.0056275	0.0056275	0.0056275	0.0056275
T_t	0.00175	0.00175	0.00175	0.00175

Since in the experiments the electric current in the forming coil is very close to an exponentially decaying sinusoid, the general form taken in the present work is

$$I(t) = I_0 \sin\left(\frac{\pi t}{2t_0}\right) \exp\left(\ln(k)\left(\frac{t}{2t_0}\right) - \frac{\ln(k)}{2}\right), \tag{5.1}$$

where $2t_0$ is the characteristic time of the current pulse, I_0 is the electric current at $t = t_0$, and k is a decay parameter, $k = -I(3t_0)/I_0$. This general form is found to give a satisfactory fit to the experimentally measured data.

In the simulations of the tall and intermediate tubes the driving input electric current in the coil has been measured experimentally (Seth, 2006), and the analytical form in Eq. (5.1) is used to find the value of the parameters I_0, t_0, and k. In the absence of experiments for the short uncoated and tall coated tubes a reasonable guess of the corresponding parameters has been made. The resulting parameter values used in the simulations are given in Table 5.

5.3.1. Expanded tubes without coating

The first tube simulation pertains to a tube taller than the forming coil. The undeformed and deformed (at maximum expansion) configurations are plotted in Fig. 5, where light gray depicts the undeformed tube and black depicts the deformed tube. Comparing the final deformed shape of the simulated tube with that in the corresponding experiment (Seth, 2006) shows that the deformed configuration is captured reasonably well.

The hoop engineering strain of the tall tube midline is plotted with respect to non-dimensional time in Fig. 6. The dimensionless currents in the coil (dashed line) and the tube (dotted line) versus the dimensionless time are also plotted in the same figure. Notice that the maximum expansion of the tube, as measured by the midline strain, peaks at $t/t_0 = 5.9$ where the currents are almost zero, well past the peaks of the first two significant current pulses at $t/t_0 = 0.8$ and 2.8. The considerable delay of maximum deformation with respect to current peak time is attributable to important inertial effects. Small amplitude elastic vibrations follow the maximum tube expansion. The period and amplitude of these vibrations agree reasonably well with recent experiments performed at The Ohio State University (Vivek and Daehn, 2008).

The electric current density in the tube for the times $t/t_0 = 0.5$, 1.3, and 2.0 is depicted in Figs. 7, 8, and 9, respectively. Note that the r-axis and z-axis have been rescaled to increase the aspect ratio of the tube's section in order to show the

Table 5
Input electric current parameters.

	Tall tube	Intermediate tube	Short tube	Coated tall tubes
I_0 (A)	137×10^3	130×10^3	117×10^3	137×10^3
t_0 (s)	17×10^{-6}	26.6×10^{-6}	26.6×10^{-6}	17×10^{-6}
k	0.3	0.3	0.3	0.3

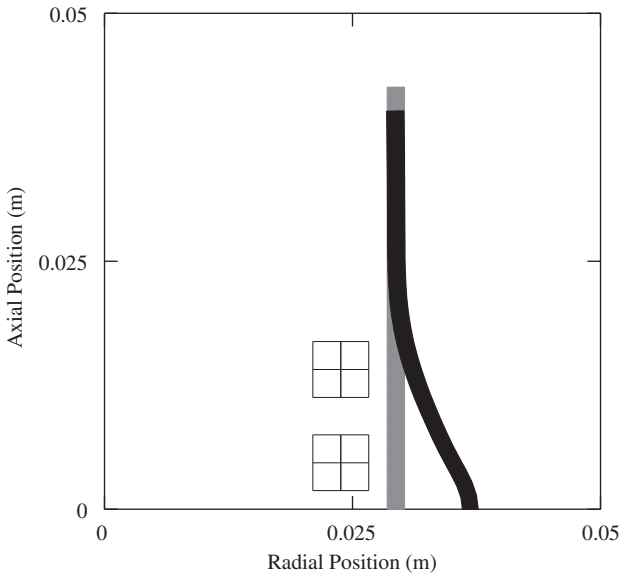

Fig. 5. Undeformed configuration (in gray) and deformed configuration (in black) at maximum midline displacement of tall tube: $t/t_0 = 5.9$.

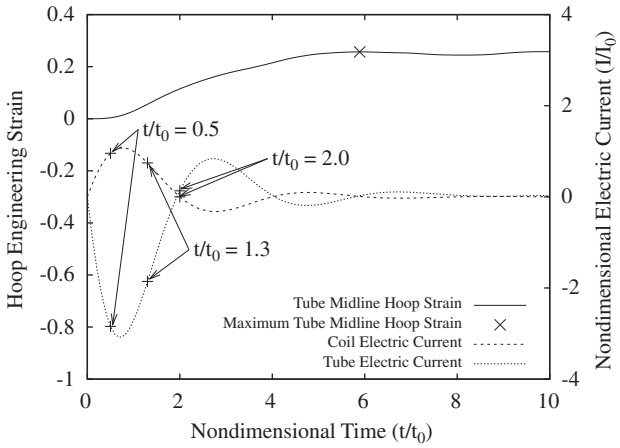

Fig. 6. Time dependence of the midline radial position and electric currents of tall tube.

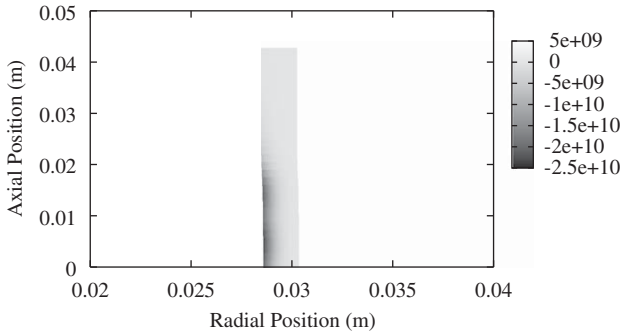

Fig. 7. Electric current density (A/m^2) distribution in the cross-section of tall tube: $t/t_0 = 0.5$.

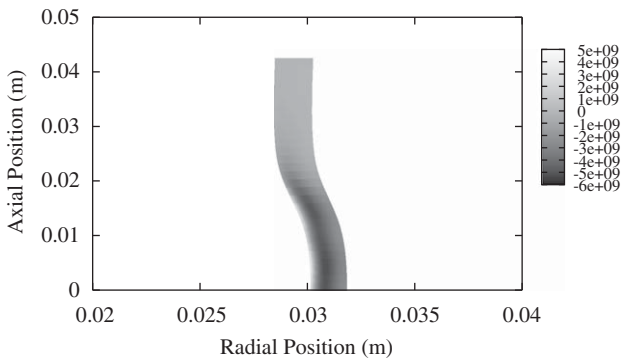

Fig. 8. Electric current density (A/m^2) distribution in the cross-section of tall tube: $t/t_0 = 1.3$.

electric current density more clearly. In Fig. 7 the electric current density at $t/t_0 = 0.5$ is plotted, which is just prior to the coil's first electric current pulse. As expected, the electric current is concentrated on the inside surface of the tube, near the coil. Note that the maximum electric current density here is negative because the corresponding coil electric current density is positive. Fig. 8 shows the electric current density at $t/t_0 = 1.3$, which is after the peak of the first current pulse of the coil. The maximum electric current density has moved from the inside surface to the middle of the tube and has decreased in intensity. In Fig. 9 the electric current density is shown at $t/t_0 = 2$, when the coil electric current is equal to zero. The electric current density distribution in the tube has already reversed from what it was initially, with Fig. 9 an inverse image of Fig. 7 (allowing for deformation) but with significantly lower intensity.

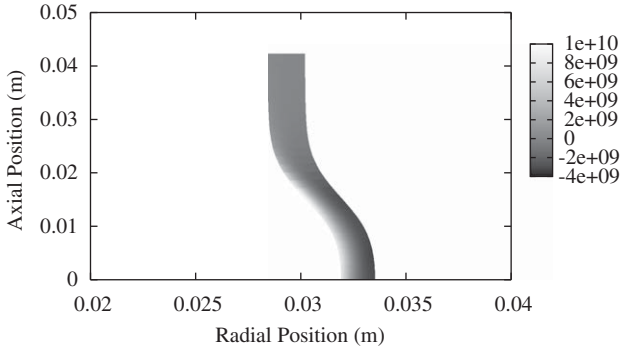

Fig. 9. Electric current density (A/m^2) distribution in the cross-section of tall tube: $t/t_0 = 2$.

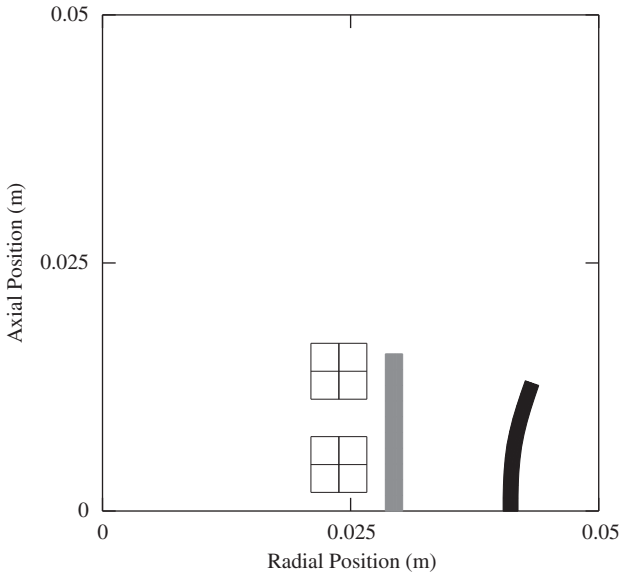

Fig. 10. Undeformed configuration (in gray) and deformed configuration (in black) at maximum midline displacement of intermediate tube: $t/t_0 = 4.5$.

The second simulation pertains to the expansion of a tube approximately the same height as the forming coil. In Fig. 10 (the counterpart of Fig. 5), the undeformed configuration is depicted in light gray and the deformed configuration is shown in black. The simulation uses an axisymmetric approximation of the experimental geometry that makes the tube slightly shorter than the coil, which produces the mildly toroidal shape. The corresponding experiments of Seth (2006) also show toroidal deformation in some specimens. In Fig. 11 (the counterpart of Fig. 6) the hoop engineering strain of the tube's midline as well as the electric currents of the coil and tube are plotted as functions of dimensionless time. The maximum expansion of the tube, as measured again by the midline strain, peaks at $t/t_0 = 4.5$, well past the peaks of the first significant current pulses, as was the case for the tall tube.

The third simulation is that of a tube much shorter than the forming coil. Fig. 12 (the counterpart of Fig. 10) shows the deformed configuration in gray and the undeformed configuration in black. The deformation qualitatively agrees with the experimentally obtained toroidal shape in the case where the tube is much shorter than the coil. In Fig. 13 (the counterpart of Fig. 11) the hoop engineering strain and electric currents are again given together. The midline strain peaks at $t/t_0 = 5.1$, well past the significant current peaks as in the previous simulations.

The three tube expansion simulations discussed above are in reasonable qualitative agreement with the experimental results of Seth (2006) and the more recent ones of Vivek and Daehn (2008). This indicates the simulation correctly captures the important aspects of the electromagnetic–mechanical interactions of free tube expansion.

5.3.2. Expanded tubes with coating

Recent work by Zhang and Ravi-Chandar (2008a) examines the effect of a polyurea coating applied to the outside surface of a freely, electromagnetically expanded ring or tube. To investigate this novel EMF problem, the fourth simulation pertains to the tall tube with hyperelastic coatings of varying thickness, with the coating modeled as either a power law

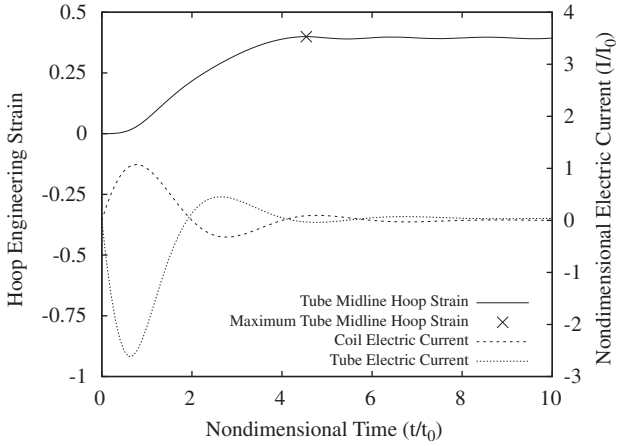

Fig. 11. Time dependence of the midline radial position and electric currents of intermediate tube.

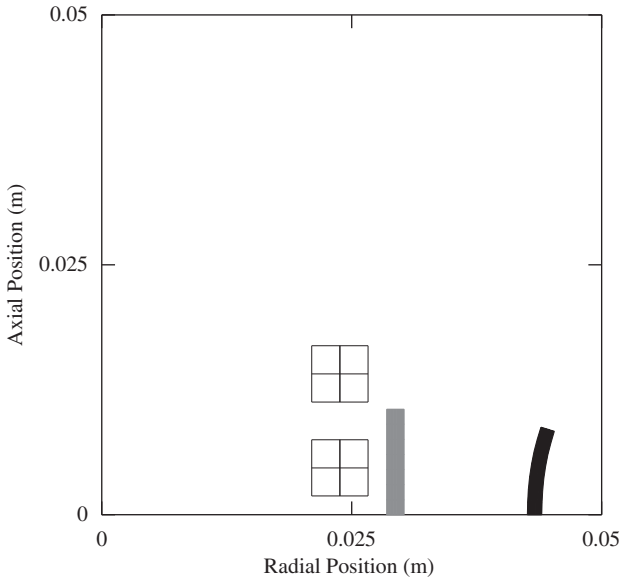

Fig. 12. Undeformed configuration (in gray) and deformed configuration (in black) at maximum midline displacement of short tube: $t/t_0 = 5.1$.

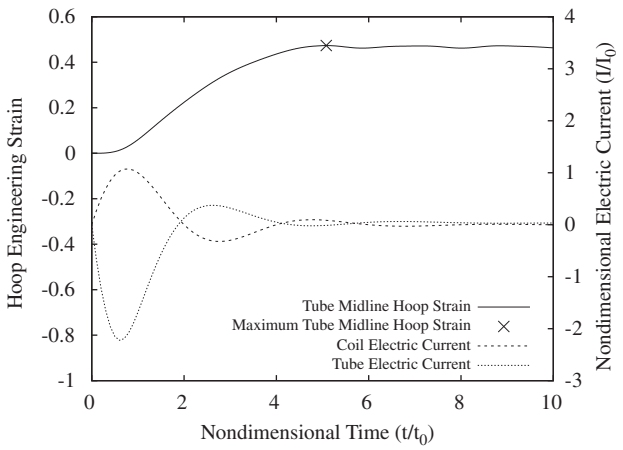

Fig. 13. Time dependence of the midline radial position and electric currents of short tube.

material (fit to polyurea uniaxial data) or a Mooney–Rivlin type material (with the same Young's modulus as the polyurea) as discussed in Section 5.2.2 and the Appendix.

As an example, in Fig. 14 the deformed midplane of the tube (excluding coating) is plotted for the case with no coating (solid line) and with a polyurea power law coating half the thickness of the tube (i.e. $T_h/T_t = 0.5$). The deformed shape is plotted at the first maximum of the midline displacement, which corresponds to approximately $t/t_0 = 5.9$ for the uncoated tube and $t/t_0 = 6.3$ for the coated tube. The maximum displacement at $Z = 0$ is significantly decreased, but the overall shape of the deformed tube is only slightly changed.

To quantify the effect of the coating we look at the maximum displacement of the tube midline (non-dimensionalized with respect to the maximum deformation without coating) versus the coating thickness (non-dimensionalized by the tube wall thickness, i.e. T_h/T_t) for each coating material. This result is given in Fig. 15. As expected, increasing the coating thickness decreases the deformation, but the difference in coating material does not have a pronounced effect. This result suggests the coating's inertia plays the major role in the decrease of displacement.

The polyurea based power law and Mooney–Rivlin results in Fig. 15 are essentially identical (with small differences attributed to numerical accuracy, due to the mesh used). This is due to the extremely low coating stiffness (relative to the aluminum tubes).

To examine the effects of coating mass density and stiffness we now vary the coating constitutive response. In one case the coating density is doubled while leaving all other material parameters as in Table 3 and in a second case the material parameters other than density are modified to make the coating stiffer. The parameters of the stiffer coating are based on the sprayed polyurea material in Chakkarapani et al. (2006), and Table 6 gives the parameters for both cases.

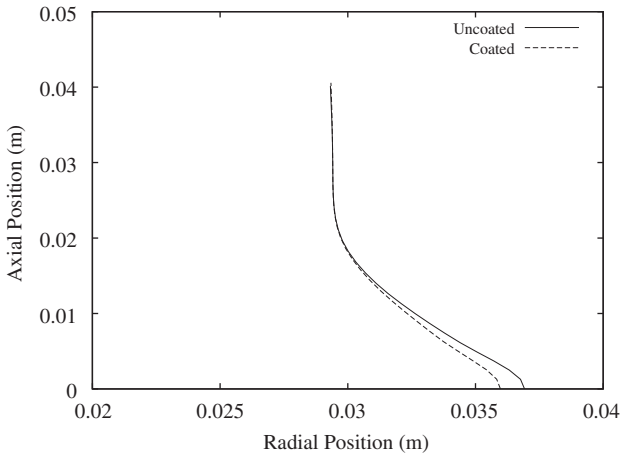

Fig. 14. Effect of (polyurea based) power law coating half the thickness of the tube on the tube midplane deformed configuration at maximum midline displacement: uncoated $t/t_0 = 5.9$, coated $t/t_0 = 6.3$.

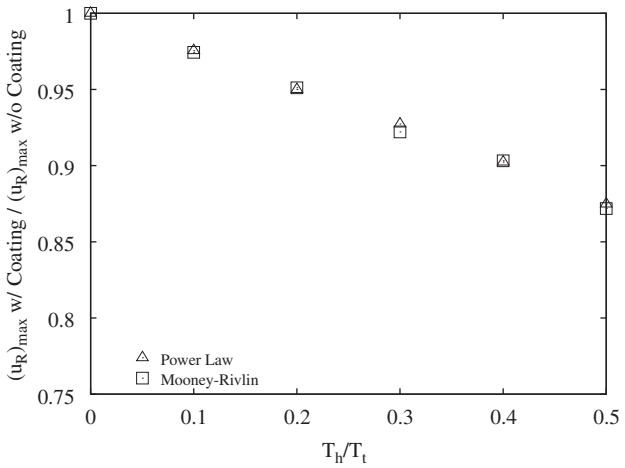

Fig. 15. Effect of coating materials on the maximum midline displacement of tall tube.

Table 6
Modified coating uniaxial mechanical constitutive parameter values.

	Increased density	Increased stiffness
E (Pa)	73×10^6	250×10^6
τ_y (Pa)	3.8×10^6	8.7×10^6
m	2.817	8.333
v	0.45	0.45
ρ_0 (kg/m^3)	2400	1200

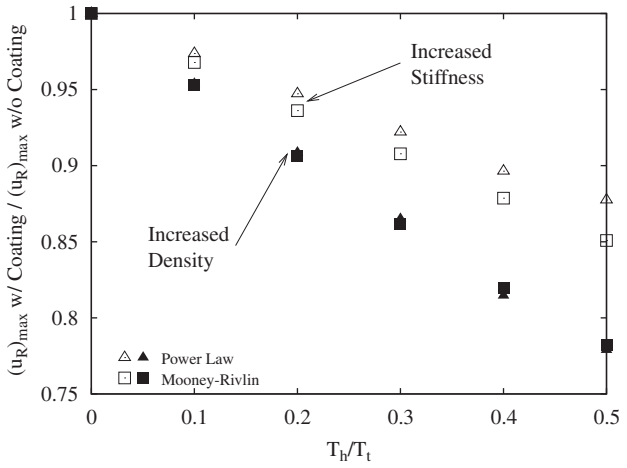

Fig. 16. Effect of modified coating materials on the maximum midline displacement of tall tube.

The results corresponding to the two cases in Table 6 are given in Fig. 16. Increasing the coating mass density significantly decreases the maximum displacement but the results from the two coating materials remain essentially identical. On the other hand, increasing the stiffness (on the order of three times stiffer) does not as greatly affect the maximum displacement but does separate the response of the two coating materials. This is due to the coating materials having different stiffening characteristics with increasing strain (see Fig. 4), and the increased stiffness of Table 6 causes this difference to be significant relative to the inertial effects.

6. Discussion

The modeling of freely expanding axisymmetric tubes has a number of simplifying assumptions that can be easily addressed within the theoretical context proposed. Moreover the present methodology can be extended to a more general class of problems involving coupled electromagnetic–mechanical processes.

To begin, the mechanical constitutive models in this work have been idealized as hyperelastic materials (coating) and as finite strain J_2 deformation theory of plasticity with unloading (metallic tube). The mechanical response of the workpiece and coatings can be more accurately captured by other elasto-plastic, elasto-visco-plastic, or thermo-visco-plastic material constitutive models, which will allow quantitative comparisons with experiments, a task in progress by the authors.

The simulations' coil electric current is assumed to be known a priori through independent measurement. Modeling the forming circuit would be useful for predicting the coil current. Implementing a capacitor circuit coupled to the FEM solution is straightforward, and the authors have already produced results with such a circuit.

The efficiency of the simulations may be improved by combining the FEM technique, applied to the nonlinear, complex solids, with a boundary element method, applied to the air where a linear equation holds for the H field, thus avoiding the need to mesh the air with deforming finite elements and to mesh a large domain to approximate the infinity boundary conditions. Other researchers currently use such techniques (L'Eplattenier et al., 2006), making these ideas a promising direction for future work.

There are several other phenomena that are associated with the free expansion of tubes that have not been presently addressed, such as localization of deformation, stability, and energy partition. One may implement the strain localization

modeling of Thomas et al. (2007) and/or relevant inertial effects into the formulation here to produce more accurate predictions of ductility in EMF expansion processes. Other forms of failure can also be explored, in particular those under electromagnetic compression of tubes that require stability considerations to investigate ovalization and collapse.

Simulation of more complex geometry problems might require a 3-D implementation. The general theory presented up to Section 3.1 is applicable to any electromagnetic–thermal–mechanical process that admits the eddy current approximation, while Sections 3.2, 4, and 5 develop an axisymmetric implementation for the processes of interest in this work. However, a 3-D implementation is necessary to predict the transition of axisymmetric problems to non-axisymmetric deformation and failure (Zhang and Ravi-Chandar, 2006). Even more generally, some aspects of the current problem, such as the helicity of the coil, must be analyzed in 3-D, and many problems of industrial interest, e.g. the electromagnetic forming of fuel cell plates (Bradley et al., 2005), have 3-D features not captured by the present analysis.

7. Conclusion

Of interest is the modeling of EMF processes, a task requiring the solution of coupled electromagnetic–mechanical (and thermal, as necessary) problems, where the governing equations are Maxwell's equations in solids—under the eddy current approximation—and Newton's equations. The present work is motivated by the need for a consistent, fully coupled variational formulation that should also lead to an efficient numerical algorithm. Past work in modeling EMF processes has not been based on such a unified variational framework nor provided adequate justification for the algorithms employed.

The present work introduces a fully coupled, reference configuration-based least-action variational principle involving a magnetic flux potential and the displacement field as independent variables. The corresponding Euler–Lagrange equations are Maxwell's and Newton's equations in the reference configuration, which are shown to coincide with their current configuration counterparts obtained independently by a direct approach. Moreover, this variational principle, combined with a variational integration numerical scheme, provides an efficient staggered solution algorithm. The proposed formulation is illustrated with simulations of the free electromagnetic expansion of uncoated and coated tubes. Although the simulation geometries, material properties, and process characteristics are borrowed to a large extent from experiments, the main goal is to demonstrate with the help of realistic examples the applicability of the general theory.

The general formulation proposed can be applicable to other related areas, besides EMF. One such possibility is the modeling of microelectromechanical devices (e.g. Li and Aluru, 2002). Another area of interest pertains to electroactive materials with magnetization and/or polarization. In particular, problems involving magnetic field-responsive polymers and elastomers (Kankanala and Triantafyllidis, 2004, 2008; Filipcsei et al., 2007) could be investigated by considering a magnetization-dependent free energy. We believe that the variational formulation proposed here and the resulting efficient discretization algorithm can be the starting point for the study of many interesting problems in the rapidly growing area of coupled electromagnetic–mechanical processes.

Acknowledgments

The authors gratefully acknowledge support from the National Science Foundation, Grant DMI 0400143, and General Motors Research and Development. The authors also acknowledge many helpful discussions with Dr. John R. Bradley of General Motors Research and Development, Professor K. Ravi-Chandar of the Aerospace Engineering and Engineering Mechanics Department at the University of Texas at Austin, Professor Glenn S. Daehn (and his research group) of The Ohio State University's Department of Materials Science and Engineering, Dr. Pierre L'Eplattenier of Livermore Software Technology Corporation, and Professor Eric Michielssen of The University of Michigan's Department of Electrical Engineering and Computer Science.

Appendix A. Mechanical constitutive models

For initially isotropic, rate independent metallic materials undergoing large strain proportional loading, a finite strain version of J_2 deformation theory of plasticity has been shown to produce reasonably accurate experimental predictions (Anand, 1979). Although this theory can accommodate any uniaxial response, a piecewise power law uniaxial response will be employed here for simplicity, namely

$$\frac{\varepsilon}{\varepsilon_y}=\frac{\tau}{\tau_y} \text{ for } \tau\leqslant\tau_y, \quad \frac{\varepsilon}{\varepsilon_y}=\left(\frac{\tau}{\tau_y}\right)^m \text{ for } \tau>\tau_y, \tag{A.1}$$

where ε is the uniaxial logarithmic strain, ε_y is the logarithmic yield strain, τ is the uniaxial mechanical Kirchhoff stress, τ_y is the mechanical Kirchhoff yield stress, and m is the hardening exponent. The logarithmic yield strain ε_y is related to the mechanical Kirchhoff yield stress τ_y by $\varepsilon_y=\tau_y/E$, where E is Young's modulus. The corresponding 3-D model used by

Abeyaratne and Triantafyllidis (1981) will be employed, i.e.

$$\rho_0\psi \equiv E\varepsilon_y^2\left[\frac{\chi}{\chi+1}\left(\frac{\tau_e}{\tau_y}\right)^{\chi+1} - \frac{1-2\nu}{6}\left(\frac{\tau_e}{\tau_y}\right)^2\right] + \frac{E}{6(1-2\nu)}(\varepsilon_1+\varepsilon_2+\varepsilon_3)^2 + G,$$
$$\frac{\varepsilon_e}{\varepsilon_y} = \left(\frac{\tau_e}{\tau_y}\right)^{\chi} - \frac{1-2\nu}{3}\left(\frac{\tau_e}{\tau_y}\right), \quad \chi = \begin{cases} 1 & \text{for } \varepsilon_e \leqslant \dfrac{2(1+\nu)}{3}\varepsilon_y, \\ m & \text{for } \varepsilon_e > \dfrac{2(1+\nu)}{3}\varepsilon_y, \end{cases} \tag{A.2}$$

where ν is Poisson's ratio, $\varepsilon_i = \ln(\lambda_i)$ are the principal logarithmic strains (λ_i are the principal stretch ratios), and G is a constant resulting from continuity of $\rho_0\psi$ at the yield point. In the above expressions the equivalent mechanical Kirchhoff stress τ_e is given in terms of the principal values τ_i of the mechanical Kirchhoff stress tensor $\boldsymbol{\tau}_m$ by

$$\tau_e \equiv \tfrac{1}{2}(\tau_1^2+\tau_2^2+\tau_3^2-\tau_1\tau_2-\tau_2\tau_3-\tau_3\tau_1)^{1/2}, \tag{A.3}$$

while the equivalent logarithmic strain ε_e is

$$\varepsilon_e \equiv \tfrac{2}{3}(\varepsilon_1^2+\varepsilon_2^2+\varepsilon_3^2-\varepsilon_1\varepsilon_2-\varepsilon_2\varepsilon_3-\varepsilon_3\varepsilon_1)^{1/2}. \tag{A.4}$$

From Eqs. (2.30), (A.1)–(A.4) the relation between the mechanical Kirchhoff stress $\boldsymbol{\tau}_m$ and the deformation gradient $\boldsymbol{F}$

$$\boldsymbol{\tau}_m = \rho_0 \frac{\partial\psi}{\partial \boldsymbol{F}} \bullet \boldsymbol{F}^T \tag{A.5}$$

can be shown (Abeyaratne and Triantafyllidis, 1981) to result due to isotropy in the following principal axes relationship:

$$\frac{1-2\nu_s}{E_s} = \frac{1-2\nu}{E}, \quad E_s = \frac{\tau}{\varepsilon}, \quad \varepsilon_e = \frac{2}{3}(1+\nu_s)\varepsilon,$$
$$\tau_i = \frac{E_s}{1+\nu_s}\left(\varepsilon_i + \frac{\nu_s}{1-2\nu_s}(\varepsilon_1+\varepsilon_2+\varepsilon_3)\right), \tag{A.6}$$

where the secant Young's modulus E_s and secant Poisson's ratio ν_s are defined such that Eqs. $(A.6)_1$, $(A.6)_2$, and $(A.6)_3$ hold.

Due to the inevitable presence of unloading, a simple extension of the model is hereby introduced. The proposed model could be cast as a one internal variable model, in accordance with the general theory presented earlier. However, an evolution law is not needed in this case, since a simpler formulation is possible. Once unloading has started, i.e. once $\tau_e < \tau_e^{\max}$ where $\tau_e^{\max}$ is the maximum value of the equivalent stress prior to the onset of unloading at the point in question, the material is assumed to continue unloading according to isotropic linear elasticity and the mechanical Kirchhoff stress is given by

$$\boldsymbol{\tau}_m = \boldsymbol{\tau}_m^{\max} + \boldsymbol{L}_{\bullet}^{\bullet}\Delta\boldsymbol{\varepsilon}_F, \tag{A.7}$$

where $\boldsymbol{\tau}_m^{\max}$ is the mechanical Kirchhoff stress at $\tau_e^{\max}$ and $\Delta\boldsymbol{\varepsilon}_F$ is the unloading part of the current configuration logarithmic strain based on the change in $\boldsymbol{F}$. This is given by

$$\Delta\boldsymbol{\varepsilon}_F \equiv \ln((\Delta\boldsymbol{F}\bullet\Delta\boldsymbol{F}^T)^{1/2}), \quad \Delta\boldsymbol{F} \equiv \boldsymbol{F}\bullet\boldsymbol{F}_{\max}^{-1}, \tag{A.8}$$

where $\boldsymbol{F}_{\max}$ is the deformation gradient at $\tau_e^{\max}$. Also, $\boldsymbol{L}$ are the linear, isotropic elastic moduli, given by

$$L_{ijkl} = \lambda\delta_{ij}\delta_{kl} + \mu(\delta_{ik}\delta_{jl} + \delta_{il}\delta_{jk}), \tag{A.9}$$

where λ and μ are the Lamé constants.

To investigate alternative coatings for the tall tube, a compressible Mooney–Rivlin hyperelastic material response is also implemented. The strain energy density is given by

$$\rho_0\psi \equiv A(I_1-3) + B(I_2-3) + C(I_3^{-2}-1) + D(I_3-1)^2, \tag{A.10}$$

where I_1, I_2, and I_3 are the invariants of the right Cauchy–Green tensor $\boldsymbol{C}$ and A, B, C, and D are material constants given by

$$A = \frac{E}{8(1+\nu)}, \quad B = A, \quad C = \frac{1}{2}A + B, \quad D = \frac{A(5\nu-2)+B(11\nu-5)}{2(1-2\nu)}. \tag{A.11}$$

References

Abeyaratne, R., Triantafyllidis, N., 1981. On the emergence of shear bands in plane strain. International Journal of Solids and Structures 17 (12), 1113–1134.

Anand, L., 1979. On H. Hencky's approximate strain-energy function for moderate deformations. ASME Journal of Applied Mechanics 46, 78–82.

Balanethiram, V., Daehn, G., 1992. Enhanced formability of interstitial free iron at high strain rates. Scripta Metallurgica et Materialia 27, 1783–1788.

Balanethiram, V., Daehn, G., 1994. Hyperplasticity: increased forming limits at high workpiece velocity. Scripta Metallurgica et Materialia 31, 515–520.

Bradley, J.R., Schroth, J.G., Daehn, G.S., 2005. Electromagnetic formation of fuel cell plates. Patent US 2005/0217334 A1.

Chakkarapani, V., Ravi-Chandar, K., Liechti, K.M., 2006. Characterization of multiaxial constitutive properties of rubbery polymers. Journal of Engineering Materials and Technology 128 (4), 489–494.

Coleman, B.D., Noll, W., 1963. The thermodynamics of elastic materials with heat conduction and viscosity. Archive for Rational Mechanics and Analysis 13 (1), 167–178.
El-Azab, A., Garnich, M., Kapoor, A., 2003. Modeling of the electromagnetic forming of sheet metals: state-of-the-art and future needs. Journal of Materials Processing Technology 142, 744–754.
Eringen, A.C., Maugin, G.A., 1990. Electrodynamics of Continua. Springer, New York.
FEAP, 2005. Finite Element Analysis Program. University of California at Berkeley (Civil and Environmental Engineering) and University of Michigan (Aerospace Engineering), Available at ⟨ http://www.ce.berkeley.edu/~rlt/feap/⟩.
Fenton, G.K., Daehn, G.S., 1998. Modeling of electromagnetically formed sheet metal. Journal of Materials Processing Technology 75, 6–16.
Filipcsei, G., Csetneki, I., Szilágyi, A., Zrínyi, M., 2007. Magnetic field-responsive smart polymer composites. In: Advances in Polymer Science, vol. 206. Springer, Berlin, pp. 137–189.
Gourdin, W.H., 1989. Analysis and assessment of electromagnetic ring expansion as a high-strain-rate test. Journal of Applied Physics 65 (2), 411–422.
Hallquist, J.O. (Ed.), 2006. LS-Dyna Theory Manual. Livermore Software Technology Corp., Available at ⟨http://www2.lstc.com/pdf/ls-dyna_theory_manual_2006.pdf⟩.
Hiptmair, R., Ostrowski, J., 2005. Coupled boundary-element scheme for eddy-current computation. Journal of Engineering Mathematics 51, 231–250.
Imbert, J., Worswick, M., Winkler, S., Golovashchenko, S., Dmitriev, V., 2005a. Analysis of the increased formability of aluminum alloy sheet formed using electromagnetic forming. In: Sheet/Hydro/Gas Forming Technology and Modeling 2005. SAE International.
Imbert, J.M., Winkler, S.L., Worswick, M.J., Oliveira, D.A., Golovashchenko, S.F., 2005b. The effect of tool-sheet interaction on damage evolution in electromagnetic forming of aluminum alloy sheet. Journal of Engineering Materials and Technology—Transactions of the ASME 127, 145–153.
Kankanala, S.V., Triantafyllidis, N., 2004. On finitely strained magnetorheological elastomers. Journal of the Mechanics and Physics of Solids 52, 2869–2908.
Kankanala, S.V., Triantafyllidis, N., 2008. Magnetoelastic buckling of a rectangular block in plane strain. Journal of the Mechanics and Physics of Solids 56, 1147–1169.
Karch, C., Roll, K., 2005. Transient simulation of electromagnetic forming of aluminum tubes. Advanced Materials Research 6–8, 639–648.
Kleiner, M., Brosius, A., Blum, H., Suttmeier, F., Stiemer, M., Svendsen, B., Unger, J., Reese, S., 2004. Benchmark simulation for coupled electromagnetic–mechanical metal forming processes. Annals of the German Society for Production Technology XI/1, 85–90.
Kovetz, A., 2000. Electromagnetic Theory. Oxford University Press, Oxford, UK.
Lax, M., Nelson, D., 1976. Maxwell equations in material form. Physical Review B 13 (4), 1777–1784.
Lazzari, B., Nibbi, R., 2000. Variational principles in electromagnetism. IMA Journal of Applied Mathematics 65, 45–95.
L'Eplattenier, P., Cook, G., Ashcraft, C., Burger, M., Shapiro, A., Daehn, G., Seth, M., 2006. Introduction of an electromagnetism module in LS-DYNA for coupled mechanical-thermal-electromagnetic simulations. In: Proceedings from 9th International LS-DYNA Users Conference, Livermore Software Technology Corp., Dearborn, MI.
Li, G., Aluru, N.R., 2002. A Lagrangian approach for electrostatic analysis of deformable conductors. Journal of Microelectromechanical Systems 11 (3), 245–254.
Lubliner, J., 1990. Plasticity Theory. Macmillan, New York.
Marsden, J.E., West, M., 2001. Discrete mechanics and variational integrators. Acta Numerica 10, 357–514.
Maugin, G.A., 1988. Continuum Mechanics of Electromagnetic Solids. North-Holland, Amsterdam.
Maugin, G.A., 1993. Material Inhomogeneities in Elasticity. Chapman & Hall, London.
Nelson, D.F., 1979. Electric, Optic, and Acoustic Interactions in Dielectrics. Wiley, New York, NY.
Oliveira, D.A., Worswick, M.J., Finn, M., Newman, D., 2005. Electromagnetic forming of aluminum alloy sheet: free-form and cavity fill experiments and model. Journal of Materials Processing Technology 170, 350–362.
Reese, S., Svendsen, B., Stiemer, M., Unger, J., Schwarze, M., Blum, H., 2005. On a new finite element technology for electromagnetic metal forming processes. Archive of Applied Mechanics 74, 834–845.
Rieben, R., Wallin, B., White, D., 2006. Arbitrary lagrangian Eulerian electromechanics in 3D. In: Proceedings of the Progress in Electromagnetics Research Symposium, Cambridge, MA, pp. 265–269.
Seth, M., 2006. High velocity formability and factors affecting it. Ph.D. Thesis, The Ohio State University, Materials Science and Engineering Department, Columbus, OH.
Seth, M., Daehn, G.S., 2005. Effect of aspect ratio on high velocity formability of aluminum alloy. In: Bieler, T.R., Carsley, J.E., Fraser, H.L., Sears, J.W., Smugeresky, J.E. (Eds.), Materials Processing and Manufacturing Division Sixth Global Innovations Proceedings. Trends in Materials and Manufacturing Technologies for Transportation Industries and Powder Metallurgy Research and Development in the Transportation Industry. TMS, pp. 59–64.
Seth, M., Vohnout, V.J., Daehn, G.S., 2005. Formability of steel sheet in high velocity impact. Journal of Materials Processing Technology 168, 390–400.
Stiemer, S., Unger, J., Svendsen, B., Blum, H., 2006. Algorithmic formulation and numerical implementation of coupled electromagnetic-inelastic continuum models for electromagnetic metal forming. International Journal for Numerical Methods in Engineering 68, 1301–1328.
Svendsen, B., Chanda, T., 2005. Continuum thermodynamic formulation of models for electromagnetic thermoinelastic solids with application in electromagnetic metal forming. Continuum Mechanics and Thermodynamics 17, 1–16.
Takatsu, N., Kato, M., Sato, K., Tobe, T., 1988. High-speed forming of metal sheets by electromagnetic force. JSME International Journal 31 (1), 142–148.
Thomas, J.D., Seth, M., Daehn, G.S., Bradley, J.R., Triantafyllidis, N., 2007. Forming limits for electromagnetically expanded aluminum alloy tubes: Theory and experiment. Acta Materialia 55, 2863–2873.
Triantafyllidis, N., Waldenmyer, J., 2004. Onset of necking in electro-magnetically formed rings. Journal of the Mechanics and Physics of Solids 52, 2127–2148.
Trimarco, C., 2007. Material electromagnetic fields and material forces. Archive of Applied Mechanics 77 (2–3), 177–184.
Trimarco, C., Maugin, G.A., 2001. Material mechanics of electromagnetic solids. In: Configurational Mechanics of Materials. CISM Courses and Lectures, No. 427. Springer, Wien, NY, pp. 129–171.
Unger, J., Stiemer, M., Svendsen, B., Blum, H., 2006. Multifield modeling of electromagnetic metal forming processes. Journal of Materials Processing Technology 177, 270–273.
Vivek, A., Daehn, G., 2008. Unpublished work.
Zhang, H., Ravi-Chandar, K., 2006. On the dynamics of necking and fragmentation—I. Real-time and post-mortem observations in Al 6061-O. International Journal of Fracture 142, 183–217.
Zhang, H., Ravi-Chandar, K., 2008a. Private communication.
Zhang, H., Ravi-Chandar, K., 2008b. On the dynamics of necking and fragmentation—II. Effect of material properties, geometrical constraints and absolute size. International Journal of Fracture 150, 3–36.